JEM-2010 transmission electron microscope at an acceleration voltage of 100 kV.

Cryo-electron microscopy

The 2D crystals were embedded in 14% trehalose[58] on Mo grids using the carbon sandwich method.[59] Excess buffer was removed by pipetting and blotting with filter paper, and then the grid was manually plunged into liquid nitrogen. These operations were carried out at 4 °C. Electron micrographs were recorded on a JEOL JEF3000SFF with a liquid helium stage cooled to a temperature of 4 K[60] at an acceleration voltage of 300 kV. Images were recorded on KODAK SO-163 films at a nominal magnification of 40,000× with an exposure time of 2 s. Defocus values used were 10,000–25,000 Å. The quality of micrographs was checked by optical diffraction, and good images were scanned by a ZEISS SCAI scanner at a 7-μm step size.

Image processing

Well-ordered areas of 5000×5000 to 10,000×10,000 pixels were used for the analysis. Filtering and unbending digitized images were performed using the MRC package.[61] Symmetry was determined as $p22_12_1$ based on the result of the *allspace* program from the MRC package. $p22_12_1$ symmetry was confirmed when each image was processed as having p1 symmetry (without assuming higher symmetry). Images were merged by refining parameters for origin, scale, tilt axis, tilt angle, and beam tilt. For the lattice constant, $c=200$ Å was used, but the density was assumed to exist within a width of 120 Å. Handedness was confirmed as described previously.[62]

Rigid-body refinement

Residues 31–104 (helices B+C), 123–142 (helix E), 147–166 (helix F), and 214–233 (helix G) were extracted as one rigid body, and residues 251–306 (helices J+K) were extracted as another rigid body from the coordinates of the ClC transporter (Protein Data Bank code 1OTS).[49] All residues other than G, P, and A are trimmed up to the C^{β} atom and treated as A (alanine) for later refinement. Rigid-body refinement was performed using CNS.[63]

Structural comparison

In Fig. 6a, the second motifs (residues 251–306) of the dimer were aligned using the program LSQMAN‡. For Fig. 6b and c, all motifs (residues 32–104 and 251–306) of the dimer were used for the alignment. The distance between loop B–C loops in the dimer was measured using the N73 residues of each monomer. The distance between loop J–K loops is measured using residue G286. The width in the z-direction was measured using the difference in z-height between N73 and G286.

Multiple sequence alignment

Sequences were fetched from public databases by PSI-BLAST[64] using the sequences of AE1 (B3AT_HUMAN) and ClC (CLCA_ECOLI) transporters to initiate the search. Next, sequences were aligned using CLUSTAL W[65] and adjusted manually if necessary. Twenty-eight sequences from the AE family and six sequences from the ClC family were selected; the sequences used are well diverged and aligned without ambiguity within each family (Supplementary Fig. 4).

The characteristics of each site are assigned based on the alignment of 28 sequences of the AE family, regardless of sequences of the ClC family. Sites that include at least one charged residue (R, K, D, or E) are marked as "charged" sites. Sites that include at least one typical hydrophobic residue (V, I, L, or M), are limited only to hydrophobic residues (V, I, L, M, G, A, and F), and are mutated twice or more are marked as "variable hydrophobic" (variphobic) sites.[56] Sites that include at least one tiny residue (G, A, or P) and are limited only to small residues (G, A, P, S, T, and C) are marked as "small residue" sites.

Accession number

The Electron Microscopy Data Bank§ accession number for the density map of AE1 is EMD-1645.

Acknowledgements

This work was supported by the Japan New Energy and Industrial Technology Development Organization. We thank Ms. T. Ogata for technical assistance. We also thank Drs. Y. Hiroaki and Y. Fujiyoshi for help with electron microscopy.

Supplementary Data

Supplementary data associated with this article can be found, in the online version, at doi:10.1016/j.jmb.2010.01.027

References

1. Fairbanks, G., Steck, T. L. & Wallach, D. F. (1971). Electrophoretic analysis of the major polypeptides of the human erythrocyte membrane. *Biochemistry*, **10**, 2606–2617.
2. Chang, S. H. & Low, P. S. (2003). Identification of a critical ankyrin-binding loop on the cytoplasmic domain of erythrocyte membrane band 3 by crystal structure analysis and site-directed mutagenesis. *J. Biol. Chem.* **278**, 6879–6884.
3. Pasternack, G. R., Anderson, R. A., Leto, T. L. & Marchesi, V. T. (1985). Interactions between protein 4.1 and band 3. An alternative binding site for an element of the membrane skeleton. *J. Biol. Chem.* **260**, 3676–3683.
4. Rybicki, A. C., Schwartz, R. S., Hustedt, E. J. & Cobb, C. E. (1996). Increased rotational mobility and extractability of band 3 from protein 4.2-deficient erythrocyte membranes: evidence of a role for protein 4.2 in strengthening the band 3–cytoskeleton linkage. *Blood*, **88**, 2745–2753.

‡ http://xray.bmc.uu.se/usf/

§ http//www.ebi.ac.uk/pdbe-srv/emsearch/index.html

5. Zhang, D., Kiyatkin, A., Bolin, J. T. & Low, P. S. (2000). Crystallographic structure and functional interpretation of the cytoplasmic domain of erythrocyte membrane band 3. *Blood*, **96**, 2925–2933.
6. Vince, J. W. & Reithmeier, R. A. (2000). Identification of the carbonic anhydrase II binding site in the Cl^-/HCO_3^- anion exchanger AE1. *Biochemistry*, **39**, 5527–5533.
7. Hamasaki, N. & Yamamoto, M. (2000). Red blood cell function and blood storage. *Vox Sang.* **79**, 191–197.
8. Romero, M. F., Hediger, M. A., Boulpaep, E. L. & Boron, W. F. (1997). Expression cloning and characterization of a renal electrogenic Na^+/HCO_3^- cotransporter. *Nature*, **387**, 409–413.
9. Takano, J., Noguchi, K., Yasumori, M., Kobayashi, M., Gajdos, Z., Miwa, K. *et al.* (2002). *Arabidopsis* boron transporter for xylem loading. *Nature*, **420**, 337–340.
10. Passow, H. (1986). Molecular aspects of band 3 protein-mediated anion transport across the red blood cell membrane. *Rev. Physiol., Biochem. Pharmacol.* **103**, 61–203.
11. Nanri, H., Hamasaki, N. & Minakami, S. (1983). Affinity labeling of erythrocyte band 3 protein with pyridoxal 5-phosphate. Involvement of the 35,000-dalton fragment in anion transport. *J. Biol. Chem.* **258**, 5985–5989.
12. Ortwein, R., Oslender-Kohnen, A. & Deuticke, B. (1994). Band 3, the anion exchanger of the erythrocyte membrane, is also a flippase. *Biochim. Biophys. Acta*, **1191**, 317–323.
13. Casey, J. R. & Reithmeier, R. A. (1991). Analysis of the oligomeric state of band 3, the anion transport protein of the human erythrocyte membrane, by size exclusion high performance liquid chromatography. Oligomeric stability and origin of heterogeneity. *J. Biol. Chem.* **266**, 15726–15737.
14. Colfen, H., Boulter, J. M., Harding, S. E. & Watts, A. (1998). Ultracentrifugation studies on the transmembrane domain of the human erythrocyte anion transporter band 3 in the detergent $C_{12}E_8$. *Eur. Biophys. J.* **27**, 651–655.
15. Lemieux, M. J., Reithmeier, R. A. & Wang, D. N. (2002). Importance of detergent and phospholipid in the crystallization of the human erythrocyte anion-exchanger membrane domain. *J. Struct. Biol.* **137**, 322–332.
16. Van Dort, H. M., Moriyama, R. & Low, P. S. (1998). Effect of band 3 subunit equilibrium on the kinetics and affinity of ankyrin binding to erythrocyte membrane vesicles. *J. Biol. Chem.* **273**, 14819–14826.
17. Wrong, O., Bruce, L. J., Unwin, R. J., Toye, A. M. & Tanner, M. J. (2002). Band 3 mutations, distal renal tubular acidosis, and Southeast Asian ovalocytosis. *Kidney Int.* **62**, 10–19.
18. Kittanakom, S., Cordat, E. & Reithmeier, R. A. (2008). Dominant-negative effect of Southeast Asian ovalocytosis anion exchanger 1 in compound heterozygous distal renal tubular acidosis. *Biochem. J.* **410**, 271–281.
19. Shami, Y., Rothstein, A. & Knauf, P. A. (1978). Identification of the Cl^- transport site of human red blood cells by a kinetic analysis of the inhibitory effects of a chemical probe. *Biochim. Biophys. Acta*, **508**, 357–363.
20. Okubo, K., Kang, D., Hamasaki, N. & Jennings, M. L. (1994). Red blood cell band 3. Lysine 539 and lysine 851 react with the same H_2DIDS (4,4′-diisothiocyanodihydrostilbene-2,2′-disulfonic acid) molecule. *J. Biol. Chem.* **269**, 1918–1926.
21. Jin, X. R., Abe, Y., Li, C. Y. & Hamasaki, N. (2003). Histidine-834 of human erythrocyte band 3 has an essential role in the conformational changes that occur during the band 3-mediated anion exchange. *Biochemistry*, **42**, 12927–12932.
22. Izuhara, K., Okubo, K. & Hamasaki, N. (1989). Conformational change of band 3 protein induced by diethyl pyrocarbonate modification in human erythrocyte ghosts. *Biochemistry*, **28**, 4725–4728.
23. Jennings, M. L., Anderson, M. P. & Monaghan, R. (1986). Monoclonal antibodies against human erythrocyte band 3 protein. Localization of proteolytic cleavage sites and stilbenedisulfonate-binding lysine residues. *J. Biol. Chem.* **261**, 9002–9010.
24. Wainwright, S. D., Tanner, M. J., Martin, G. E., Yendle, J. E. & Holmes, C. (1989). Monoclonal antibodies to the membrane domain of the human erythrocyte anion transport protein. Localization of the C-terminus of the protein to the cytoplasmic side of the red cell membrane and distribution of the protein in some human tissues. *Biochem. J.* **258**, 211–220.
25. Hamasaki, N., Okubo, K., Kuma, H., Kang, D. & Yae, Y. (1997). Proteolytic cleavage sites of band 3 protein in alkali-treated membranes: fidelity of hydropathy prediction for band 3 protein. *J. Biochem.* **122**, 577–585.
26. Abe, Y., Chaen, T., Jin, X. R., Hamasaki, T. & Hamasaki, N. (2004). Mass spectrometric analyses of transmembrane proteins in human erythrocyte membrane. *J. Biochem.* **136**, 97–106.
27. Popov, M., Tam, L. Y., Li, J. & Reithmeier, R. A. (1997). Mapping the ends of transmembrane segments in a polytopic membrane protein. Scanning N-glycosylation mutagenesis of extracytosolic loops in the anion exchanger, band 3. *J. Biol. Chem.* **272**, 18325–18332.
28. Popov, M., Li, J. & Reithmeier, R. A. (1999). Transmembrane folding of the human erythrocyte anion exchanger (AE1, band 3) determined by scanning and insertional N-glycosylation mutagenesis. *Biochem. J.* **339**, 269–279.
29. Kanki, T., Sakaguchi, M., Kitamura, A., Sato, T., Mihara, K. & Hamasaki, N. (2002). The tenth membrane region of band 3 is initially exposed to the luminal side of the endoplasmic reticulum and then integrated into a partially folded band 3 intermediate. *Biochemistry*, **41**, 13973–13981.
30. Tang, X. B., Fujinaga, J., Kopito, R. & Casey, J. R. (1998). Topology of the region surrounding Glu681 of human AE1 protein, the erythrocyte anion exchanger. *J. Biol. Chem.* **273**, 22545–22553.
31. Fujinaga, J., Tang, X. B. & Casey, J. R. (1999). Topology of the membrane domain of human erythrocyte anion exchange protein, AE1. *J. Biol. Chem.* **274**, 6626–6633.
32. Zhu, Q., Lee, D. W. & Casey, J. R. (2003). Novel topology in C-terminal region of the human plasma membrane anion exchanger, AE1. *J. Biol. Chem.* **278**, 3112–3120.
33. Groves, J. D., Wang, L. & Tanner, M. J. (1998). Functional reassembly of the anion transport domain of human red cell band 3 (AE1) from multiple and non-complementary fragments. *FEBS Lett.* **433**, 223–227.
34. Groves, J. D. & Tanner, M. J. (1999). Structural model for the organization of the transmembrane spans of the human red-cell anion exchanger (band 3; AE1). *Biochem. J.* **344**, 699–711.
35. Ota, K., Sakaguchi, M., Hamasaki, N. & Mihara, K. (1998). Assessment of topogenic functions of anticipated transmembrane segments of human band 3. *J. Biol. Chem.* **273**, 28286–28291.

36. Ota, K., Sakaguchi, M., Hamasaki, N. & Mihara, K. (2000). Membrane integration of the second transmembrane segment of band 3 requires a closely apposed preceding signal-anchor sequence. *J. Biol. Chem.* **275**, 29743–29748.
37. Li, C., Takazaki, S., Jin, X., Kang, D., Abe, Y. & Hamasaki, N. (2006). Identification of oxidized methionine sites in erythrocyte membrane protein by liquid chromatography/electrospray ionization mass spectrometry peptide mapping. *Biochemistry*, **45**, 12117–12124.
38. Jennings, M. L. & Anderson, M. P. (1987). Chemical modification and labeling of glutamate residues at the stilbenedisulfonate site of human red blood cell band 3 protein. *J. Biol. Chem.* **262**, 1691–1697.
39. Kalo, M. S. (1996). Topological disposition of tyrosine 486 in anion exchanger from human erythrocytes. *Biochemistry*, **35**, 999–1009.
40. Takazaki, S., Abe, Y., Kang, D., Li, C., Jin, X., Ueda, T. & Hamasaki, N. (2006). The functional role of arginine 901 at the C-terminus of the human anion transporter band 3 protein. *J. Biochem.* **139**, 903–912.
41. Kuma, H., Shinde, A. A., Howren, T. R. & Jennings, M. L. (2002). Topology of the anion exchange protein AE1: the controversial sidedness of lysine 743. *Biochemistry*, **41**, 3380–3388.
42. Kuma, H., Abe, Y., Askin, D., Bruce, L. J., Hamasaki, T., Tanner, M. J. & Hamasaki, N. (2002). Molecular basis and functional consequences of the dominant effects of the mutant band 3 on the structure of normal band 3 in Southeast Asian ovalocytosis. *Biochemistry*, **41**, 3311–3320.
43. Wang, L., Groves, J. D., Mawby, W. J. & Tanner, M. J. (1997). Complementation studies with co-expressed fragments of the human red cell anion transporter (band 3; AE1). The role of some exofacial loops in anion transport. *J. Biol. Chem.* **272**, 10631–10638.
44. Popov, M., Tam, L. Y., Li, J. & Reithmeier, R. A. (1997). Mapping the ends of transmembrane segments in a polytopic membrane protein. *J. Biol. Chem.* **272**, 18325–18332.
45. Wang, D. N., Sarabia, V. E., Reithmeier, R. A. & Kühlbrandt, W. (1994). Three-dimensional map of the dimeric membrane domain of the human erythrocyte anion exchanger, band 3. *EMBO J.* **13**, 3230–3235.
46. Yamaguchi, T., Fujii, T., Abe, Y., Hirai, T., Kang, D., Namba, K. *et al.* (2009). Helical image reconstruction of the outward-open human erythrocyte band 3 membrane domain in tubular crystals. *J. Struct. Biol.*, doi:10.1016/j.jsb.2009.12.009.
47. Jentsch, T. J., Friedrich, T., Schriever, A. & Yamada, H. (1999). The CLC chloride channel family. *Pflugers Arch.* **437**, 783–795.
48. Dutzler, R., Campbell, E. B., Cadene, M., Chait, B. T. & MacKinnon, R. (2002). X-ray structure of a ClC chloride channel at 3.0 Å reveals the molecular basis of anion selectivity. *Nature*, **415**, 287–294.
49. Dutzler, R., Campbell, E. B. & MacKinnon, R. (2003). Gating the selectivity filter in ClC chloride channels. *Science*, **300**, 108–112.
50. Accardi, A. & Miller, C. (2004). Secondary active transport mediated by a prokaryotic homologue of ClC Cl^- channels. *Nature*, **427**, 803–807.
51. Miller, C. & White, M. M. (1984). Dimeric structure of single chloride channels from Torpedo electroplax. *Proc. Natl Acad. Sci. USA*, **81**, 2772–2775.
52. Mindell, J. A., Maduke, M., Miller, C. & Grigorieff, N. (2001). Projection structure of a ClC-type chloride channel at 6.5 Å resolution. *Nature*, **409**, 219–223.
53. Collaborative Computational Project, Number 4. (1994). The CCP4 suite: programs for protein crystallography. *Acta Crystallogr., Sect. D: Biol. Crystallogr.* **50**, 760–763.
54. Potterton, L., McNicholas, S., Krissinel, E., Gruber, J., Cowtan, K., Emsley, P. *et al.* (2004). Developments in the CCP4 molecular-graphics project. *Acta Crystallogr., Sect. D: Biol. Crystallogr.* **60**, 2288–2294.
55. Taylor, A. M., Zhu, Q. & Casey, J. R. (2001). Cysteine-directed cross-linking localizes regions of the human erythrocyte anion-exchange protein (AE1) relative to the dimeric interface. *Biochem. J.* **359**, 661–668.
56. Taylor, W. R., Jones, D. T. & Green, N. M. (1994). A method for alpha-helical integral membrane protein fold prediction. *Proteins*, **18**, 281–294.
57. Kang, D., Okubo, K., Hamasaki, N., Kuroda, N. & Shiraki, H. (1992). A structural study of the membrane domain of band 3 by tryptic digestion. Conformational change of band 3 *in situ* induced by alkali treatment. *J. Biol. Chem.* **267**, 19211–19217.
58. Hirai, T., Murata, K., Mitsuoka, K., Kimura, Y. & Fujiyoshi, Y. (1999). Trehalose embedding technique for high-resolution electron crystallography: application to structural study on bacteriorhodopsin. *J. Electron Microsc.* **48**, 653–658.
59. Gyobu, N., Tani, K., Hiroaki, Y., Kamegawa, A., Mitsuoka, K. & Fujiyoshi, Y. (2004). Improved specimen preparation for cryo-electron microscopy using a symmetric carbon sandwich technique. *J. Struct. Biol.* **146**, 325–333.
60. Fujiyoshi, Y., Mizusaki, T., Morikawa, K., Yamagishi, H., Aoki, Y., Kihara, H. & Harada, Y. (1991). Development of a superfluid-helium stage for high-resolution electron-microscopy. *Ultramicroscopy*, **38**, 241–251.
61. Crowther, R. A., Henderson, R. & Smith, J. M. (1996). MRC image processing programs. *J. Struct. Biol.* **116**, 9–16.
62. Hirai, T., Heymann, J. A., Shi, D., Sarker, R., Maloney, P. C. & Subramaniam, S. (2002). Three-dimensional structure of a bacterial oxalate transporter. *Nat. Struct. Biol.* **9**, 597–600.
63. Brunger, A. T., Adams, P. D., Clore, G. M., DeLano, W. L., Gros, P., Grosse-Kunstleve, R. W. *et al.* (1998). Crystallography & NMR System: a new software suite for macromolecular structure determination. *Acta Crystallogr., Sect. D: Biol. Crystallogr.* **54**, 905–921.
64. Altschul, S. F., Madden, T. L., Schaffer, A. A., Zhang, J., Zhang, Z., Miller, W. & Lipman, D. J. (1997). Gapped BLAST and PSI-BLAST: a new generation of protein database search programs. *Nucleic Acids Res.* **25**, 3389–3402.
65. Thompson, J. D., Higgins, D. G. & Gibson, T. J. (1994). CLUSTAL W: improving the sensitivity of progressive multiple sequence alignment through sequence weighting, position-specific gap penalties and weight matrix choice. *Nucleic Acids Res.* **22**, 4673–4680.

Journal of Structural Biology 169 (2010) 406–412

Contents lists available at ScienceDirect

Journal of Structural Biology

journal homepage: www.elsevier.com/locate/yjsbi

Helical image reconstruction of the outward-open human erythrocyte band 3 membrane domain in tubular crystals

Tomohiro Yamaguchi [a,1], Takashi Fujii [b], Yoshito Abe [c], Teruhisa Hirai [a], Dongchon Kang [d], Keiichi Namba [b], Naotaka Hamasaki [e,*], Kaoru Mitsuoka [f,*]

[a] RIKEN SPring-8 Center, Harima Institute, Hyogo, Japan
[b] Graduate School of Frontier Biosciences, Osaka University, Osaka, Japan
[c] Graduate School of Pharmaceutical Sciences, Kyushu University, Fukuoka, Japan
[d] Graduate School of Medical Sciences, Kyushu University, Fukuoka, Japan
[e] Faculty of Pharmaceutical Sciences, Nagasaki International University, Nagasaki, Japan
[f] Biomedicinal Information Research Center, National Institute of Advanced Industrial Science and Technology, Tokyo, Japan

ARTICLE INFO

Article history:
Received 11 September 2009
Received in revised form 7 December 2009
Accepted 7 December 2009
Available online 21 December 2009

Keywords:
Band 3
Membrane protein structure
Cryo-electron microscopy
Tubular crystal
Iterative helical real-space reconstruction

ABSTRACT

The C-terminal membrane domain of erythrocyte band 3 functions as an anion exchanger. Here, we report the three-dimensional (3D) structure of the membrane domain in an inhibitor-stabilized, outward-open conformation at 18 Å resolution. Unstained, frozen-hydrated tubular crystals containing the membrane domain of band 3 purified from human red blood cells (hB3MD) were examined using cryo-electron microscopy and iterative helical real-space reconstruction (IHRSR). The 3D image reconstruction of the tubular crystals showed the molecular packing of hB3MD dimers with dimensions of 60 × 110 Å in the membrane plane and a thickness of 70 Å across the membrane. Immunoelectron microscopy and carboxyl-terminal digestion demonstrated that the intracellular surface of hB3MD was exposed on the outer surface of the tubular crystal. A 3D density map revealed that hB3MD consists of at least two subdomains and that the outward-open form is characterized by a large hollow area on the extracellular surface and continuous density on the intracellular surface.

1. Introduction

Erythrocyte band 3 (anion exchanger 1, or AE1) is a polytopic membrane protein that mediates electroneutral exchange of such ions as chloride and bicarbonate across the erythrocyte plasma membrane. Because of its biological importance and abundance in red blood cells, band 3 has been extensively studied as an integral membrane protein, especially as an excellent model of transporters (Casey and Reithmeier, 1998; Tanner, 1997). For example, the anion transport mechanism of band 3 has been explained by a "ping-pong" model (Gunn and Fröhlich, 1979; Knauf, 1979; Furuya et al., 1984; Passow, 1986). This model postulates that there is only one transport site, which faces either intracellularly (inward-open form) or extracellularly (outward-open form). Conformational changes between these forms only occur if a substrate is bound to the transport site.

Band 3 contains functionally independent cytoplasmic and membrane domains. Whereas the 40-kDa NH_2-terminal cytoplasmic domain (amino acids 1–360) functions to anchor the cytoskeleton to the plasma membrane (Low, 1986), the 55-kDa C-terminal membrane domain (hB3MD; amino acids 361–911) allows anion exchange (Lepke et al., 1992). Band 3 exists as a mixture of dimers and tetramers; most of the protein in membranes or nonionic detergent solution is a dimer (Casey and Reithmeier, 1991), although the monomer is also able to transport anions (Lindenthal and Schubert, 1991). The isolated membrane domain exists exclusively as a stable dimer, because tetramer formation requires the NH_2-terminal cytoplasmic domain (Casey and Reithmeier, 1991; Wang et al., 1994).

Despite significant effort, the structure of the band 3 membrane domain remains unclear. The atomic structure of the cytoplasmic domain, on the other hand, was revealed using X-ray crystallography (Zhang et al., 2000). To date, however, the structure of the membrane domain has only been observed at 20 Å resolution following electron crystallographic analysis of negatively stained two-dimensional (2D) crystals (Wang et al., 1994). Even the

* Corresponding authors. Addressess: Faculty of Pharmaceutical Sciences, Nagasaki International University, 2825-7 Huis Ten Bosch-cho, Sasebo, Nagasaki 859-3298, Japan (N. Hamasaki); Biomedicinal Information Research Center, National Institute of Advanced Industrial Science and Technology, 2-41-6 Aomi, Koto-ku, Tokyo 135-0064, Japan (K. Mitsuoka). Fax: +81 3 3599 8099 (K. Mitsuoka), +81 956 20 5622 (N. Hamasaki).
E-mail addresses: hamasaki-nao@niu.ac.jp (N. Hamasaki), kaorum@ni.aist.go.jp (K. Mitsuoka).
[1] Present address: Department of Structural Biology, Graduate School of Pharmaceutical Sciences, Kyoto University, Kyoto, Japan.

1047-8477/$ - see front matter © 2009 Elsevier Inc. All rights reserved.
doi:10.1016/j.jsb.2009.12.009

topology of the membrane domain has remained to be unclear. (Fujinaga et al., 1999; Hamasaki et al., 1997; Kuma et al., 2002a; Popov et al., 1997, 1998; Zhu et al., 2003). More detailed information about the structure of the membrane domain and relevant conformational changes is required for a full understanding of the anion transport mechanism.

hB3MD can be prepared using mild trypsin treatment of erythrocyte membranes (Lepke et al., 1992; Lepke and Passow, 1976). We purified hB3MD with the anion transport inhibitor 4,4′-diisothiocyanatodihydrostilbene-2,2′-disulfonic acid (H_2DIDS). It has been reported that stilbene compounds, such as DIDS and H_2DIDS, stabilize band 3 in the outward-open form (Shami et al., 1978; Barzilay et al., 1979), and that DIDS increases the thermal stability of band 3 (Appell and Low, 1982). H_2DIDS efficiently reacts with Lys539 and Lys851 of band 3 at alkaline pH levels, resulting in intramolecular cross-linking (Jennings and Passow, 1979; Okubo et al., 1994). Using purified H_2DIDS-bound, outward-open hB3MD and a dialysis procedure, we obtained tubular crystals with a diameter of 37 nm.

IHRSR uses single-particle image analysis in combination with imposed real-space helical symmetry to allow effective analysis of tubular crystals with such properties as a poorly ordered helical symmetry, bent tubes, or low signal-to-noise ratios on electron microscopy images (Egelman, 2000, 2007). The structures of various membrane proteins in tubular crystals, including a Ca^{2+}-ATPase and a Na^+/K^+-ATPase, have been analyzed using the IHRSR method (Pomfret et al., 2007; Rice et al., 2001; Stokes et al., 2005). Here, we report the 3D structure of the hB3MD dimer in the outward-open form at 18 Å resolution, which was obtained using cryo-electron microscopy image analysis of unstained, frozen-hydrated tubular crystals and IHRSR.

2. Materials and methods

2.1. Materials

TPCK-trypsin (sequence grade) and *N*-glycosidase F were purchased from Roche Diagnostics (Mannheim, Germany). H_2DIDS was purchased from Molecular Probes (Oregon, USA). A POROS-HQ/20 anion-exchange column was purchased from Applied Biosystems (California, USA). DEAE Sepharose Fast Flow resin was purchased from GE Healthcare UK (Buckinghamshire, UK). Octaethylene glycol monododecyl ether ($C_{12}E_8$) was purchased from Wako Co. (Osaka, Japan). Octaethylene glycol tridecyl ether (ANAPOE-$C_{13}E_8$; $C_{13}E_8$) was purchased from Anatrace (Ohio, USA). 1,2-Dioleoyl-*sn*-glycero-3-phospho-L-ethanolamine (DOPE) was purchased from Sigma Aldrich (Missouri, USA). Carboxypeptidase Y (CPY) was purchased from Oriental Yeast Co. (Osaka, Japan). Five nanometers gold-conjugated, anti-mouse goat IgG was purchased from BBInternational (Cardiff, UK).

2.2. Purification of hB3MD from human blood cells

Human blood stored at 4 °C in acid/citrate/dextrose solution was obtained from the Fukuoka Red Cross Blood Center. Red-cell membranes (white ghosts) were prepared as described previously (Kang et al., 1992). White ghosts (~400 mg) were incubated with H_2DIDS (2 mg) in 10 mM borate buffer (pH 9.5) at 37 °C for 90 min. To remove the 40-kDa NH_2-terminal domain of band 3, the membranes were treated with TPCK-trypsin (0.4 mg) in 5 mM Na_2CO_3 for 30 min on ice. Peripheral membrane proteins were stripped using 10 mM NaOH. Membrane proteins were simultaneously solubilized with 0.1% (v/v) $C_{12}E_8$ and deglycosylated with *N*-glycosidase F (100 U) for 24 h at room temperature. Solubilized hB3MD was then HPLC purified using a POROS-HQ/20 anion-exchange column; elution was performed with a 0–0.84 M gradient of NaCl (BioCAD 700E perfusion chromatography). Purified hB3MD was concentrated using the batch method and DEAE Sepharose resin; for this step, the detergent $C_{12}E_8$ was exchanged with $C_{13}E_8$.

2.3. Preparation of tubular crystals

Purified hB3MD in 0.1% (w/v) $C_{13}E_8$ was mixed with DOPE prepared in 2% (w/v) $C_{13}E_8$ such that the lipid–protein ratios (LPR) ranged from 0.125 to 0.175 and the final protein concentration was 1.0 mg/ml. The mixtures were dialyzed in a dialysis button, initially against 10 mM Tris (pH 8.0), 100 mM NaCl, and 0.02% NaN_3 at 20 °C for 8 days, and then against 10 mM Tris (pH 8.0), 20 mM NaCl, 10 mM $Na_4P_2O_7$, and 0.02% NaN_3 at 20 °C for 5 days. The crystallization efficiency was better with this two-step dialysis procedure, which first used buffer without and then with $Na_4P_2O_7$, probably because $Na_4P_2O_7$ tends to denature hB3MD in detergent micelles although it stabilizes tubular crystals. Similar tubular crystals were not obtained with $C_{12}E_8$ as a detergent (data not shown). Because membrane proteins are normally inserted randomly into lipid bilayers, hB3MD molecules may interact with each other during reconstruction with $C_{13}E_8$ and DOPE, resulting in a consistent orientation in lipid bilayers and the subsequent growth of tubular crystals.

2.4. Electron microscopy

To screen tubular crystallization conditions, samples were negatively stained with 2% uranyl acetate. To determine the handedness of the tubular crystals, a modified negative-staining method was used. Tubular crystal samples were mixed with trehalose (final concentration, 5%) and applied onto copper grids covered with a thin carbon film. After excess liquid was absorbed, the sample on the grid was partially dried and stained with 2% uranyl acetate.

For immunoelectron microscopy, the crystal samples were washed via two cycles of centrifugation at 3000*g* for 2 min and suspension in distilled water. The washed samples were incubated in 100 mM NaOH on ice for 30 min, followed by three cycles of centrifugation and suspension, and addition of CPY buffer (20 mM sodium phosphate buffer at pH 6.5). The samples were then incubated with 0.1 mg CPY/mg hB3MD in CPY buffer at room temperature overnight. CPY-treated and -untreated crystal samples were applied to the grids. The grids were then twice washed with buffer (10 mM Tris–HCl and 150 mM NaCl at pH 8.0), followed by incubation at room temperature for 2 h with 1.0 mg/ml 2A8 mouse IgG antibodies, which were specific for a C-terminal peptide (DEYDEVAMPV) from band 3. The grids were then washed twice, incubated with colloidal gold-conjugated anti-mouse goat IgG antibodies at room temperature for 1 h, washed three times, and stained with 2% uranyl acetate.

The samples were examined using a JEM-1010 or JEM-2010 transmission electron microscope (JEOL, Tokyo, Japan) operated at 100 kV.

2.5. Cryo-electron microscopic image data collection and analysis using IHRSR

The crystal samples were diluted in crystallization buffer, and placed on copper grids covered with a thin, holey carbon film. After blotting with filter paper, each grid was quickly frozen by plunging it into liquid ethane. The frozen specimens were transferred into a JEM-Z2100 or JEM-3100FFC electron microscope (JEOL, Tokyo, Japan) operated at an acceleration voltage of 200 kV or 300 kV, respectively. Both microscopes were equipped with a field emission gun and liquid helium-cooled specimen stage. The specimens

were cooled to a temperature of 4 K, and images of the tubular crystals embedded in vitreous ice over the holes in the carbon film were recorded on SO-163 film (Kodak, Rochester, NY) at a magnification of 50,000× with a 2-s exposure and underfocus by approximately 2 μm. The images were digitized at a step size of 7 μm with a SCAI scanner (Zeiss, Thornwood, NY), after which the image size was reduced using 2 × 2 binning to save computing time. Well-ordered tubes were selected using the Helixboxer program from EMAN (Ludtke et al., 1999). The defocus values for each image were determined using CTFFIND3 (Mindell and Grigorieff, 2003).

The spacing of the layer lines from the cryo-electron microscopic images of hB3MD tubular crystals was measured using comparisons with the strongest layer line of tobacco mosaic virus (TMV) particles (23 Å) in the same images. The spacing of the strongest layer line of the hB3DM tubular crystal was determined to be 48.0 Å, and the effective magnifications of the micrographs recorded at accelerating voltages of 200 and 300 kV were determined to be 49,100× and 54,900×, respectively. The pixel size of 300 kV electron microscopic images was adjusted to match that of the 200 kV electron microscopic images (2.85 Å/pixel).

Cryo-electron microscopic images of the tubular crystals were segmented along the helical axis into a series of square images with dimensions of 200 × 200 pixels and a relative shift of six pixels using the Boxer program from EMAN (Fig. 2A), resulting in one large data set. Prior to refinement with IHRSR analysis, each subimage was temporarily and coarsely aligned against a projection generated from a preliminary reconstructed map of the tubular crystal, and then was used for multireference alignments. The actual alignment interpolation was performed for each of the original subimages as described below. After flipping the CTF phases, the data set was analyzed as follows. First, a set of projection images was generated from a reference 3D map in different azimuthal angles around the tube axis. Second, each coarsely aligned subimage underwent multireference alignment against the reference projections. Third, the 3D volume was generated from back projections of the aligned subimages. Fourth, we searched for helical symmetry in the asymmetric 3D volume, and imposed any identified symmetry. Finally, we corrected for the CTF amplitude by weighting the amplitudes calculated and averaged using the defocus values from all the subimages used for the back projections (Sachse et al., 2007). The resulting 3D volume was used as a new, helical symmetry-enforced reference volume in the subsequent round of refinement. This cycle was repeated to improve the 3D map until the helical symmetry parameters ($\Delta\varphi$ and Δz) converged. In the present analysis, the reference projections were generated at 8° steps, resulting in 45 reference projections and a resolution limit of approximately 8 Å. Any further increase in the number of reference projections did not improve the resolution (data not shown). The resolution was estimated from the Fourier shell correlation (FSC) between reconstructions derived from two randomly selected halves of the data set. To measure the resolution accurately, the data set was divided such that segment images generated from the same tubular crystal belonged to the same half of the data set, and the numbers of segment images in each half set were similar.

The computational procedures for the refinement cycles were mainly written using the image processing package SPIDER (Frank et al., 1996) as well as with independent programs provided by E.H. Egelman (University of Virginia Health Sciences, USA) for the helical symmetry search of the asymmetric 3D volume and helical-symmetry imposition. The 3D density maps were visualized using Chimera (Pettersen et al., 2004).

2.6. Other methods

For immunoblotting, the samples were subjected to SDS–PAGE and transferred to nitrocellulose membranes (Schleicher and Schuell, Dassel, Germany). Membranes were then blocked with 1% BSA in TBS-T (25 mM Tris–HCl at pH 7.4, 137 mM NaCl, 3 mM KCl, and 0.003% Tween 20) for 1 h, and incubated with 2A8 IgG antibodies (1.0 μg/ml) for 3 h at room temperature. The membranes were washed with TBS-T, incubated with secondary antibodies for 1 h, washed, and visualized using BCIP/NBT substrates (Promega Biotech, Wisconsin, USA).

3. Results and discussion

3.1. Tubular crystals of hB3MD

Purified hB3MD (Fig. 1A) formed tubular crystals following dialysis of the sample solution in a mixture of DOPE and $C_{13}E_8$ micelles against buffer solutions (Fig. 1B and C). As shown in Fig. 1B, the tubular crystals appeared to grow from aggregates. In this study, we used partially deglycosylated hB3MD (Fig. 1A). Thorough deglycosylation of hB3MD resulted in similar tubular crystals without any improvement in the crystal quality (data not shown). Although negatively stained tubular crystals seemed partially flattened on the electron microscopy grid (Fig. 1C) with markedly larger diameters than those observed in cryo-electron micrographs of frozen-hydrated specimens (Fig. 2A), the Fourier transform showed a few sharp layer lines (Fig. 1D). Because the thin tubular crystals tended to bend and presumably had poorly ordered helical arrays of subunits, however, they did not show many strong layer lines. We therefore used the IHRSR method (Egelman, 2000) to carry out 3D image reconstruction of the tubular crystals.

3.2. Determination of the helical parameters and handedness

The frozen-hydrated tubular crystals showed a diameter of 37 nm on cryo-electron microscopic images (Fig. 2A). Because the

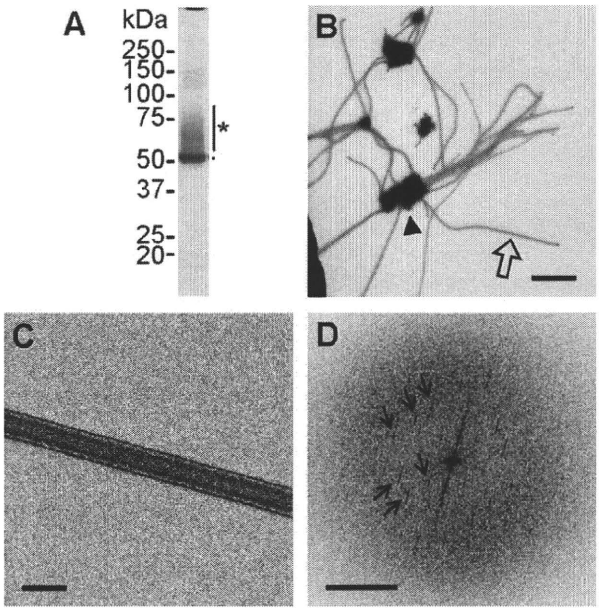

Fig. 1. Preparation and characterization of the tubular crystals. (A) Coomassie blue-stained gels following SDS–PAGE of the membrane domains of band 3 purified from human erythrocytes (hB3MD). Sharp (dot) and smeared bands (vertical bar with asterisk) correspond to deglycosylated and glycosylated hB3MD, respectively. (B) An electron micrograph showing negatively stained tubular crystals of hB3MD growing from aggregates. The tubular crystals were obtained by removing $C_{13}E_8$ from mixtures containing purified hB3MD, DOPE, and $C_{13}E_8$ via dialysis. The tubular crystals (open arrow) appear to have grown from aggregates (arrowhead). Scale bar, 2 μm. (C) A higher magnification image of an hB3MD tubular crystal. Scale bar, 100 nm. (D) Fourier transform of the image in (C). A few sharp layer lines are indicated by arrows. Scale bar, 0.025 $Å^{-1}$.

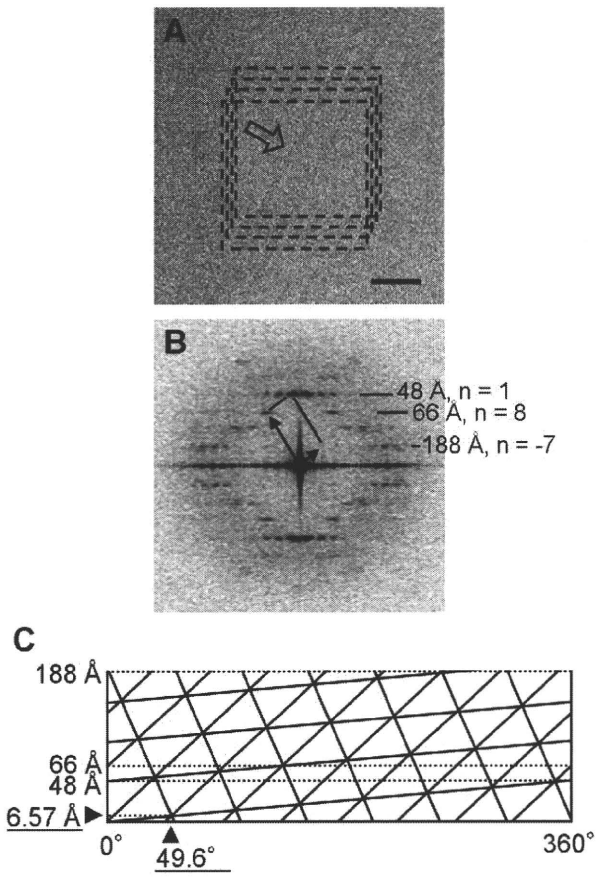

Fig. 2. Cryo-electron microscopic image of the tubular crystal, averaged Fourier transform, and cylindrical surface lattice. (A) A cryo-electron microscopic image of an hB3MD tubular crystal (open arrow). Dashed squares illustrate how the subimages were generated. Scale bar, 50 nm. (B) Averaged Fourier transform of subimages generated from 33 cryo-electron microscopic images, each of which contained a relatively straight, long tubular crystal. Each layer line was indexed as described in the text and labeled in the figure with the layer line spacing. A set of layer line peaks from one side of the tubular crystal are indicated by arrows and lines. Major layer lines with spacings of 66, 188, and 48 Å were assigned the helical index of $n = 8, -7$, and 1, respectively. (C) A cylindrical surface lattice diagram of the tubular crystal. The figure was drawn by scaling up two times in the direction of the tubular axis. The initial helical symmetry parameters were an azimuthal rotation ($\Delta\varphi$) of 49.6° and an axial rise (Δz) of 6.57 Å per subunit (arrowheads).

contrast was very low on the cryo-electron microscopic images, the layer lines in the Fourier transform of the images were too weak to analyze using conventional Fourier–Bessel methods (data not shown). Fig. 2B shows an averaged Fourier transform of 33 segment images, each of which was segmented from the original image of the tubular crystals (Fig. 2A) and oriented vertically. The layer lines became much stronger and clearly visible using this averaging procedure (Fig. 2B).

To obtain initial values for the helical symmetry parameters using the IHRSR method, we analyzed the averaged Fourier transform. Using the relationship $2\pi Rr = \sim |n| + 2$, where R is the radial distance from the meridian to the first peak of each layer line, r is the radius of the tubular crystal, and n is the helical index, major layer lines were indexed as shown in Fig. 2B (Stewart, 1988). The initial values of the helical parameters were determined to be a rotation angle per subunit ($\Delta\varphi$) of 49.6° and an axial rise (Δz) of 6.57 Å (Fig. 2C). Using these values, we applied the IHRSR method to the images. The actual magnifications of the images were determined from the spacing of the strongest layer line associated with TMV as described in Section 2.

The helical parameters converged after five cycles of refinement. After 30 cycles, $\Delta\varphi$ and Δz were 49.56° and 6.659 Å, respectively (Supplementary Fig. 1). The data set used here consisted of 8777 segment images, which contained approximately 23,000 unit cells. The resolution was estimated from the FSC between reconstructions from halves of the data set, which was randomly divided in two. Based on a cutoff value of 0.5 in the FSC, the resolution of this reconstructed 3D map was 18 Å (Supplementary Fig. 2). This resolution is similar to that of the previously reported 3D map of a 2D crystal (20 Å resolution) (Wang et al., 1994).

Although IHRSR analysis was performed with the assumption that the 1-start helix is right handed, it was necessary to confirm the handedness (Egelman, 2000). Thus, we observed the tubular crystals under electron microscopy using a negatively stained specimen that had been partially dried in trehalose (Fig. 3A). By embedding the sample in trehalose before staining, primarily the upper half of the tubular crystals was stained, which was confirmed using TMV (data not shown). The averaged Fourier transform of eight such images (Fig. 3C) showed that both the 1-start helix with a spacing of 48 Å and the 8-start helix with a spacing of 66 Å were right-handed. In agreement with this observation, the most prominent 8-start helical subunits array in the projection image of the near-side half of the 3D map (Fig. 3B) is right handed. The layer line positions in the Fourier transform of the projection image (boxes in Fig. 3D) are also the same as those found in the averaged Fourier transform (Fig. 3C). Therefore, the helical handedness we used for 3D image reconstruction was correct.

3.3. Orientation of hB3MD in the tubular crystal

To determine the orientation of hB3MD in the tubular crystal, we examined the tubular crystals using immunoelectron microscopy and 2A8 IgG antibodies, which were specific for a C-terminal

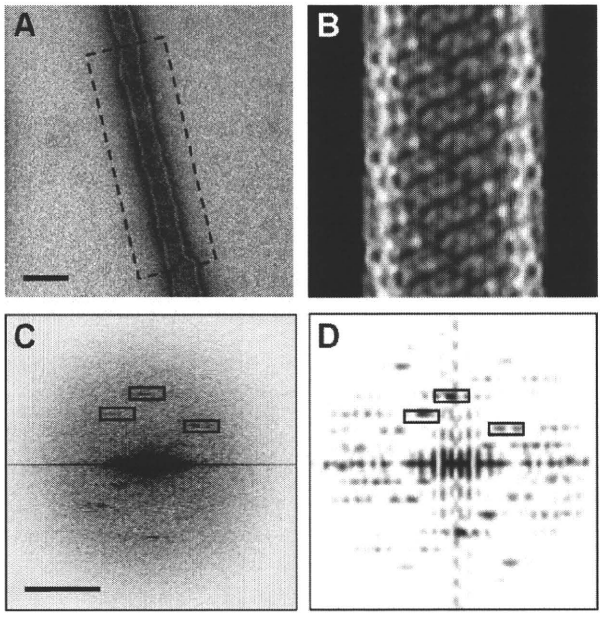

Fig. 3. Determination of the helical handedness of the tubular crystal. The tubular crystals were partially dried on grids in trehalose, negatively stained, and examined with electron microscopy to reveal the subunit helical array on the upper surface of the tube. (A) An electron microscopic image of the tubular crystal. The dashed box indicates the image area used for calculating the Fourier transform in (C). Scale bar, 100 nm. (B) A projection image of the near-side half of the 3D map after image reconstruction. A right-handed 8-start helical array of the subunits with a helical pitch of 66 Å is evident. (C) An averaged Fourier transform of eight tubular crystal images, such as the one shown in (A). Scale bar, 0.025 $Å^{-1}$. (D) Fourier transform of the image in (B). The Fourier transforms in (C and D) agree with each other, as marked by boxes, indicating that the handedness used for 3D image reconstruction was correct.

peptide from hB3MD that is known to face intracellularly (Lieberman and Reithmeier, 1988; Wainwright et al., 1989). It has been suggested that the C-terminus of hB3MD is protected within the molecule, but is exposed in response to NaOH (Mori et al., 1995; Takazaki et al., 2006). Pretreatment of crystal samples with NaOH increased the number of gold particle-conjugated antibodies that were attached to the tubes (Fig. 4A and Supplementary Figs. 3 and 4). Incubation of NaOH-treated tubular crystals with CPY to remove the C-terminal chain reduced the degree of antibody labeling (Fig. 4B and Supplementary Fig. 4). When tubular crystals were treated with CPY, the mobility of hB3MD in SDS–PAGE did not markedly change, whereas immunoblotting analysis showed reduced antibody-specific signals (Fig. 4C), indicating that CPY digested only a short C-terminal chain, which containing the antibody epitope. These results indicate that the C-terminus was exposed on the surface of the tubular crystal. We therefore concluded that hB3MD is embedded in the tubular crystal with its intracellular surface exposed on the outside of the tube.

3.4. Structural features of hB3MD

Fig. 5A shows the overall 3D map of the hB3MD tubular crystal. Two hB3MD molecules that form a dimer are marked with blue and green boxes. All of the hB3MD dimers are oriented in the same direction relative to the tube axis and appear to be in close contact with each other. Fig. 5B shows an end-on view of the 3D map. As discussed in the previous section, the outer and inner surfaces of the tubular crystal corresponded to the intracellular and extracellular portions of hB3MD, respectively. Two continuous high-density layers along the intracellular and extracellular surfaces are recognizable in the cross-section (white dashed lines in Fig. 5B); these likely represent the two membrane surfaces, because they are approximately 40 Å apart and phosphate residues from phospholipid head groups in bilayer membranes form two high-density layers separated by approximately 40 Å.

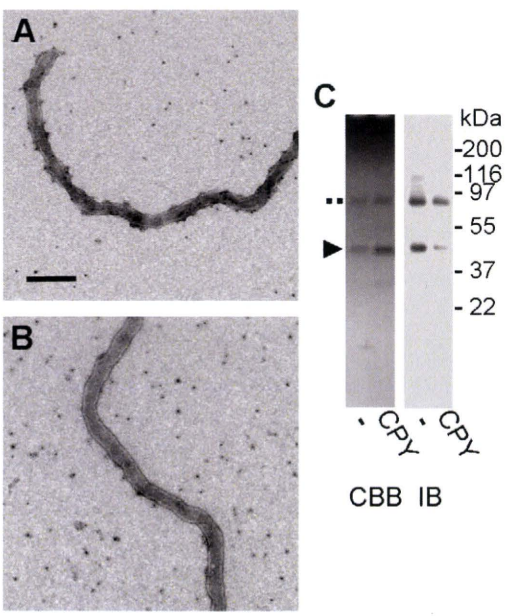

Fig. 4. Immunoelectron microscopy to determine which side of hB3MD is exposed on the outer surface of the tubular crystal. (A and B) Immunoelectron microscopy of the tubular crystals using 2A8 IgG antibodies specific for an intracellular C-terminal peptide from band 3. Gold particles (black dots) are evident on the tube in (A). Treatment with CPY before immunolabeling reduced the gold labeling on the tube in (B). Scale bar, 200 nm. (C) A coomassie blue-stained gel following SDS–PAGE (left panel; CBB) and immunoblotting (right panel; IB) of untreated (−) or CPY-treated (CPY) tubular crystal samples. Although CPY treatment did not markedly change the mobility of hB3MD during SDS–PAGE, 2A8 IgG antibody binding was reduced significantly (arrowhead). The double dot indicates the hB3MD dimer, which was probably denatured because it did not dissociate in SDS. These results suggest that the hB3MD molecule is oriented in the tubular crystal with its intracellular C-terminus exposed on the outside of the tube.

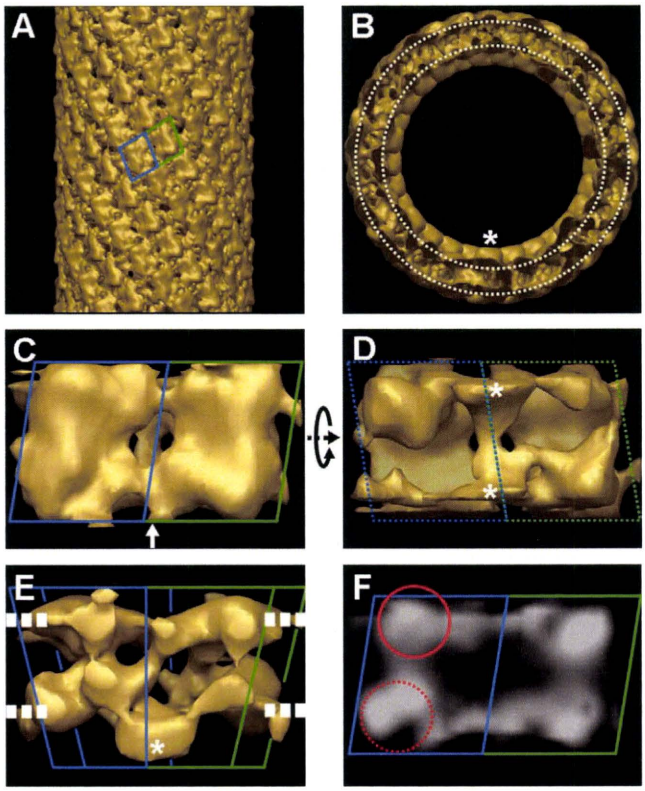

Fig. 5. Three-dimensional image reconstruction of the hB3MD tubular crystal. (A) Side view of the 3D map. Two hB3MD molecules forming a dimer are marked by blue and green boxes in (A and C) through (F). (B) End-on view of the 3D map. The predicted positions of the membrane surfaces are indicated by white dashed lines in (B and E). Protrusions on the extracellular surface with a height of 20 Å are indicated by asterisks in (B, D, and E). (C and D) The intracellular (C) and extracellular (D) surfaces of a unit cell containing an hB3MD dimer. The unit cell was cut out from the 3D map of the tubular crystal shown in (A and B). (E) The 3D map of an hB3MD dimer viewed in the direction of the arrow in (C), which is parallel to the tube axis. (F) Projection image of the 3D map shown in (C) from the intracellular side. Two high-density regions indicated by solid and dashed red circles appear to suggest the presence of two subdomains.

Fig. 5C and D shows the 3D maps of the intracellular and extracellular surfaces of a unit cell, respectively. The unit cell contains two hB3MD molecules that form a dimer (blue and green boxes in Fig. 5C and D). The hB3MD dimer occupies 60 × 110 Å in the membrane plane, which is similar to the previously reported dimensions for the 2D crystal structure (Wang et al., 1994). The hB3MD dimer appears to have approximate 2-fold symmetry, with a symmetry axis perpendicular to the membrane plane. Although the densities of the two molecules in the dimer differ, it is not clear that the conformations of the two hB3MD molecules in the dimer are actually different at this resolution (18 Å).

Fig. 5E shows the 3D map of the hB3MD dimer viewed along the tube axis, which was parallel to the membrane plane. White dashed lines denote the positions of the membrane surfaces as predicted by the continuous high-density layers, which presumably represent the phospholipid head groups. The upper and lower layers correspond to the intracellular and extracellular sides, respectively. hB3MD was 70 Å long in the direction perpendicular to the membrane, which is shorter than the previously reported value of 80 Å (Wang et al., 1994). We believe that our 3D map is more

reliable than the previous one derived from 2D crystal structure analysis, particularly along this direction, because our 3D map is not affected by a missing cone in the Fourier data collection, which is associated with 2D crystals and tends to blur the 3D map in the direction perpendicular to the plane of a 2D crystal.

The density on the intracellular surface was essentially continuous, whereas that on the extracellular surface was separated into discrete regions by a large hollow within each molecule (Fig. 5C and D). Protrusions reached 20 Å above the extracellular surface (Fig. 5B, D and E). Our 3D map presumably represents an outward-open structure of hB3MD because stilbene compounds, such as DIDS and H_2DIDS, stabilize the band 3 in this form (Shami et al., 1978; Barzilay et al., 1979). Thus, the large hollow in the extracellular density and the continuous intracellular density likely reflect an outward-open conformation of hB3MD.

Although the dimensions of our map parallel to the membrane were similar to those reported by Wang et al. (60 × 110 Å), the height of the map was shorter (70 versus 80 Å) (Wang et al., 1994). In both cases, the intracellular region of the membrane domain was larger than the extracellular region. Although our map included extracellular protrusions near the center of the dimer, the map from Wang et al. had larger intracellular protrusions in areas on the periphery of the dimer. The differences in the overall architecture of these models may be caused by H_2DIDS binding; hB3MD packing in tubular and 2D crystals; real-space reconstruction with helical symmetry versus electron crystallography of 2D crystals; or issues intrinsic to unstained cryo-electron microscopy or negative-stained electron microscopic images.

The transmembrane region of hB3MD appeared thinner than the domains on the membrane surfaces. At the present resolution of 18 Å, however, it is difficult to distinguish protein domains on the membrane surface from the continuous high-density layers formed by the phospholipid head groups; therefore, the dimensions of the molecule along the membrane plane cannot be detailed.

The membrane domain of band 3 is thought to consist of several subdomains (Hamasaki et al., 1997, 1998; Groves and Tanner, 1999; Kuma et al., 2002b). Fig. 5F is a projection image of the 3D map of the hB3MD dimer perpendicular to the membrane plane, showing the overall density distribution of each molecule and suggesting that the domain is composed of at least two subdomains. Currently, however, it is not possible to determine which segment of the molecule belongs to each subdomain.

In conclusion, the present study revealed the "native" 3D structure of an hB3MD dimer stabilized in the outward-open form using cryo-electron microscopic image analysis of frozen-hydrated tubular crystals. The 3D map showed an approximate 2-fold symmetry and suggested that the hB3MD molecule consists of at least two subdomains. To determine the relationship between the structural features revealed here and the function of band 3, a higher resolution structure is required.

Acknowledgments

We thank Yoshinori Fujiyoshi, Yoko Hiroaki, and Kazutoshi Tani for invaluable discussions. We also thank Kazumi Kobayashi (JEOL DATUM) for technical advice about cryo-electron microscopy. Xiu Ri Jin, Kayoko Tsunematsu, and Takako Ogata provided technical support during sample purification. This research was supported in part by Grants-in-Aid for Scientific Research on Priority Area 'Membrane Interface' to T.Y. and on Priority Area 'Biological Macromolecular Assemblies' to K.N. (16087207) from the Ministry of Education, Culture, Sports, Science, and Technology of Japan; and by the Japan New Energy and Industrial Technology Development Organization (NEDO) to K.M.

Appendix A. Supplementary data

Supplementary data associated with this article can be found, in the online version, at doi:10.1016/j.jsb.2009.12.009.

References

Appell, K.C., Low, P.S., 1982. Evaluation of the structural interdependence of the membrane-spanning and cytoplasmic domains of band 3. Biochemistry 21, 2151–2157.

Barzilay, M., Ship, S., Cabantchik, Z.I., 1979. Anion transport in red blood cells. I. Chemical properties of anion recognition sites as revealed by structure–activity relationships of aromatic sulfonic acids. Membr. Biochem. 2, 227–254.

Casey, J.R., Reithmeier, R.A., 1991. Analysis of the oligomeric state of band 3, the anion transport protein of the human erythrocyte membrane, by size exclusion high performance liquid chromatography. Oligomeric stability and origin of heterogeneity. J. Biol. Chem. 266, 15726–15737.

Casey, J.R., Reithmeier, R.A., 1998. Anion exchangers in the red cell and beyond. Biochem. Cell Biol. 76, 709–713.

Egelman, E.H., 2000. A robust algorithm for the reconstruction of helical filaments using single-particle methods. Ultramicroscopy 85, 225–234.

Egelman, E.H., 2007. The iterative helical real space reconstruction method, surmounting the problems posed by real polymers. J. Struct. Biol. 157, 83–94.

Frank, J., Radermacher, M., Penczek, P., Zhu, J., Li, Y., Ladjadj, M., Leith, A., 1996. SPIDER and WEB, processing and visualization of images in 3D electron microscopy and related fields. J. Struct. Biol. 116, 190–199.

Fujinaga, J., Tang, X.B., Casey, J.R., 1999. Topology of the membrane domain of human erythrocyte anion exchange protein, AE1. J. Biol. Chem. 274, 6626–6633.

Furuya, W., Tarshis, T., Law, F.Y., Knauf, P.A., 1984. Transmembrane effects of intracellular chloride on the inhibitory potency of extracellular H_2DIDS. Evidence for two conformations of the transport site of the human erythrocyte anion exchange protein. J. Gen. Physiol. 83, 657–681.

Groves, J.D., Tanner, M.J., 1999. Structural model for the organization of the transmembrane spans of the human red-cell anion exchanger (band 3; AE1). Biochem. J. 344, 699–711.

Gunn, R.B., Fröhlich, O., 1979. Asymmetry in the mechanism for anion exchange in human red blood cell membranes. Evidence for reciprocating sites that react with one transported anion at a time. J. Gen. Physiol. 74, 351–374.

Hamasaki, N., Okubo, K., Kuma, H., Kang, D., Yae, Y., 1997. Proteolytic cleavage sites of band 3 protein in alkali-treated membranes, fidelity of hydropathy prediction for band 3 protein. J. Biochem. 122, 577–585.

Hamasaki, N., Kuma, H., Ota, K., Sakaguchi, M., Mihara, K., 1998. A new concept in polytopic membrane proteins following from the study of band 3 protein. Biochem. Cell Biol. 76, 729–733.

Jennings, M.L., Passow, H., 1979. Anion transport across the erythrocyte membrane, in situ proteolysis of band 3 protein, and cross-linking of proteolytic fragments by 4,4′-diisothiocyano dihydrostilmen-2′2-disulfonate. Biochim. Biophys. Acta 554, 498–519.

Kang, D., Okubo, K., Hamasaki, N., Kuroda, N., Shiraki, H., 1992. A structural study of the membrane domain of band 3 by tryptic digestion. Conformational change of band 3 in situ induced by alkali treatment. J. Biol. Chem. 267, 19211–19217.

Knauf, P.A., 1979. Erythrocyte anion exchange and the band 3 protein, transport kinetics and molecular structure. Curr. Top. Membr. Transp. 12, 249–363.

Kuma, H., Shinde, A.A., Howren, T.R., Jennings, M.L., 2002a. Topology of the anion exchange protein AE1, the controversial sidedness of lysine 743. Biochemistry 41, 3380–3388.

Kuma, H., Abe, Y., Askin, D., Bruce, L.J., Hamasaki, T., Tanner, M.J., Hamasaki, N., 2002b. Molecular basis and functional consequences of the dominant effects of the mutant band 3 on the structure of normal band 3 in Southeast Asian ovalocytosis. Biochemistry 41, 3311–3320.

Lepke, S., Passow, H., 1976. Effects of incorporated trypsin on anion exchange and membrane proteins in human red blood cell ghost. Biochim. Biophys. Acta 455, 353–370.

Lepke, S., Becker, A., Passow, H., 1992. Mediation of inorganic anion transport by the hydrophobic domain of mouse erythroid band 3 protein expressed in oocytes of *Xenopus laevis*. Biochim. Biophys. Acta 1106, 13–16.

Lieberman, D.M., Reithmeier, R.A., 1988. Localization of the carboxyl terminus of band 3 to the cytoplasmic side of the erythrocyte membrane using antibodies raised against a synthetic peptide. J. Biol. Chem. 263, 10022–10028.

Lindenthal, S., Schubert, D., 1991. Monomeric erythrocyte band 3 protein transports anions. Proc. Natl. Acad. Sci. USA 88, 6540–6544.

Low, P.S., 1986. Structure and function of the cytoplasmic domain of band 3, center of erythrocyte membrane–peripheral protein interactions. Biochim. Biophys. Acta 864, 145–167.

Ludtke, S.J., Baldwin, P.R., Chiu, W., 1999. EMAN, semiautomated software for high-resolution single-particle reconstructions. J. Struct. Biol. 128, 82–97.

Mindell, J.A., Grigorieff, N., 2003. Accurate determination of local defocus and specimen tilt in electron microscopy. J. Struct. Biol. 142, 334–347.

Mori, A., Okubo, K., Kang, D., Hamasaki, N., 1995. A structural study of the carboxyl terminal region of the human erythrocyte band 3 protein. J. Biochem. 118, 1192–1198.

Okubo, K., Kang, D., Hamasaki, N., Jennings, M.L., 1994. Red blood cell band 3. Lysine 539 and lysine 851 react with the sameH2DIDS (4,4′-diisothio-

cyanodihydrostilbene- 2,2′-disulfonic acid) molecule. J. Biol. Chem. 269, 1918–1926.
Passow, H., 1986. Molecular aspects of band 3 protein-mediated anion transport across the red blood cell membrane. Rev. Physiol. Biochem. Pharmacol. 103, 61–203.
Pettersen, E.F., Goddard, T.D., Huang, C.C., Couch, G.S., Greenblatt, D.M., Meng, E.C., Ferrin, T.E., 2004. UCSF Chimera – a visualization system for exploratory research and analysis. J. Comput. Chem. 25, 1605–1612.
Pomfret, A.J., Rice, W.J., Stokes, D.L., 2007. Application of the iterative helical real-space reconstruction method to large membranous tubular crystals of P-type ATPases. J. Struct. Biol. 157, 106–116.
Popov, M., Tam, L.Y., Li, J., Reithmeier, R.A., 1997. Mapping the ends of transmembrane segments in a polytopic membrane protein. Scanning *N*-glycosylation mutagenesis of extracytosolic loops in the anion exchanger, band 3. J. Biol. Chem. 272, 18325–18332.
Popov, M., Li, J., Reithmeier, R.A., 1998. Transmembrane folding of the human erythrocyte anion exchanger (AE1, Band 3) determined by scanning and insertional *N*-glycosylation mutagenesis. Biochem. J. 339, 269–279.
Rice, W.J., Young, H.S., Martin, D.W., Sachs, J.R., Stokes, D.L., 2001. Structure of Na^+, K^+-ATPase at 11-A resolution, comparison with Ca^{2+}-ATPase in E1 and E2 states. Biophys. J. 80, 2187–2197.
Sachse, C., Chen, J.Z., Coureux, P.D., Stroupe, M.E., Fändrich, M., Grigorieff, N., 2007. High-resolution electron microscopy of helical specimens, a fresh look at tobacco mosaic virus. J. Mol. Biol. 371, 812–835.
Shami, Y., Rothstein, A., Knauf, P.A., 1978. Identification of Cl^- transport site of human red blood cells by kinetic analysis of the inhibitory effects of a chemical probe. Biochim. Biophys. Acta 508, 357–363.
Stewart, M., 1988. Computer image processing of electron micrographs of biological structures with helical symmetry. J. Electron. Microsc. Tech. 9, 325–358.
Stokes, D.L., Delavoie, F., Rice, W.J., Champeil, P., McIntosh, D.B., Lacapère, J.J., 2005. Structural studies of a stabilized phosphoenzyme intermediate of Ca^{2+}-ATPase. J. Biol. Chem. 280, 18063–18072.
Takazaki, S., Abe, Y., Kang, D., Li, C., Jin, X., Ueda, T., Hamasaki, N., 2006. The functional role of arginine 901 at the C-terminus of the human anion transporter band 3 protein. J. Biochem. 139, 903–912.
Tanner, M.J., 1997. The structure and function of band 3 (AE1), recent developments. Mol. Membr. Biol. 14, 155–165.
Wainwright, S.D., Tanner, M.J., Martin, G.E., Yendle, J.E., Holmes, C., 1989. Monoclonal antibodies to the membrane domain of the human erythrocyte anion transport protein. Localization of the C-terminus of the protein to the cytoplasmic side of the red cell membrane and distribution of the protein in some human tissues. Biochem. J. 258, 211–220.
Wang, D.N., Sarabia, V.E., Reithmeier, R.A., Kühlbrandt, W., 1994. Three-dimensional map of the dimeric membrane domain of the human erythrocyte anion exchanger, band 3. EMBO J. 13, 3230–3235.
Zhang, D., Kiyatkin, A., Bolin, J.T., Low, P.S., 2000. Crystallographic structure and functional interpretation of the cytoplasmic domain of erythrocyte membrane band 3. Blood 96, 2925–2933.
Zhu, Q., Lee, D.W., Casey, J.R., 2003. Novel topology in C-terminal region of the human plasma membrane anion exchanger, AE1. J. Biol. Chem. 278, 3112–3120.

5554–5568 Nucleic Acids Research, 2010, Vol. 38, No. 16 Published online 29 April 2010
doi:10.1093/nar/gkq305

ERAL1 is associated with mitochondrial ribosome and elimination of ERAL1 leads to mitochondrial dysfunction and growth retardation

Takeshi Uchiumi*, Kippei Ohgaki, Mikako Yagi, Yoshimasa Aoki, Aya Sakai, Shinya Matsumoto and Dongchon Kang*

Department of Clinical Chemistry and Laboratory Medicine, Kyushu University Graduate School of Medical Sciences, 3-1-1, Maidashi, Higashi-ku, Fukuoka 812-8582, Japan

Received August 13, 2009; Revised April 5, 2010; Accepted April 12, 2010

ABSTRACT

ERAL1, a homologue of Era protein in *Escherichia coli*, is a member of conserved GTP-binding proteins with RNA-binding activity. Depletion of prokaryotic Era inhibits cell division without affecting chromosome segregation. Previously, we isolated ERAL1 protein as one of proteins which were associated with mitochondrial transcription factor A by using immunoprecipitation. In this study, we analysed the localization and function of ERAL1 in mammalian cells. ERAL1 was localized in mitochondrial matrix and associated with mitoribosomal proteins including the 12S rRNA. siRNA knockdown of ERAL1 decreased mitochondrial translation, caused redistribution of ribosomal small subunits and reduced 12S rRNA. The knockdown of ERAL1 in human HeLa cells elevated mitochondrial superoxide production and slightly decreased mitochondrial membrane potential. The knockdown inhibited the growth of HeLa cells with an accumulation of apoptotic cells. These results suggest that ERAL1 is localized in a small subunit of the mitochondrial ribosome, plays an important role in the small ribosomal constitution, and is also involved in cell viability.

INTRODUCTION

The circular 16.5 kb human mitochondrial DNA (mtDNA) molecule encodes 2 rRNAs, 22 tRNAs and 13 proteins of the mitochondrial oxidative phosphorylation system responsible for the production of cellular ATP. All the 13 proteins are considered to be essential subunits of a mitochondrial respiratory chain. The 2 rRNAs and 22 tRNAs, used for constructing mitochondrial translational machineries, are also essential for synthesis of the proteins encoded by mtDNA (1,2). Given that majority of ATP production depends on the respiratory chain, maintenance of the mitochondrial genome is critical for individuals to maintain normal health. The mitochondrial respiratory chain consists of five complexes, composed of more than 80 structural proteins. The 13 mtDNA-encoded polypeptides are integral parts of four mitochondrial respiratory chain complexes (I, III, IV and V). Complex II is an only respiratory chain complex that lacks mtDNA-encoded subunits (3).

Synthesis of these 13 proteins is carried out on a specialized translational apparatus located in the mitochondrial matrix. Components of the mitochondrial translational machinery (translational factors, elongation factor and mitoribosomes) are considered to generally resemble the bacterial translational machinery and are distinct from those in cytosol (4,5). Mitoribosome in mammalian is a 55S particle composed of a small 28S and a large 39S subunit and contains a much higher number of proteins and RNAs than those of the bacterial 70S ribosome (6). All of ~80 mitochondrial ribosomal proteins are the products of nuclear genes and are imported into the mitochondrial matrix (7). To assemble the mitochondrial ribosome, the rRNA synthesis by the mitochondrial transcription machinery needs to coordinate with nuclear expression of the mitoribosomal proteins (6). Several mutations are reported in the nuclear-encoded translation machinery factors such as elongation factor EFG1 and mitochondrial small ribosomal protein (MRPS16 and MRPS22) of patients with autosomal recessive mitochondrial translation defects (8–11).

Mammalian cells contain up to thousands of copies of mtDNA. mtDNAs are organized in nucleoids (12,13). Mitochondrial transcription factor A (TFAM), which

*To whom correspondence should be addressed. Tel: +81 92 642 5752; Fax: +81 92 642 5772; Email: uchiumi@cclm.med.kyushu-u.ac.jp
Correspondence may also be addressed to Dongchon Kang. Tel: +81 92 642 5748; Fax: +81 92 642 5772; Email: kang@cclm.med.kyushu-u.ac.jp

was cloned as a transcription factor for mtDNA (14), has known to be essential for the maintenance of mtDNA. mtDNA molecules are packaged into nucleoids. TFAM may be a main factor for the packaging (15). The nucleoids may dynamically change their structure and distribution within mitochondria undergoing fission and fusion and are involved in a variety of dynamic processes including mitochondrial replication, transcription and translation (16). Previously, we isolated ERAL1 as a protein associated with TFAM (17).

In *Escherichia coli*, Era (*E. coli* Ras-like protein), is an essential GTP-binding protein and exchanges guanine nucleotide rapidly within seconds (18,19). Era leads to accumulation of an unprocessed precursor of the 16S rRNA. It is shown by electron microscopy that Era locates to the cleft between the head and the platform of the 30S small ribosomal subunit. Furthermore, Era makes contacts with the several assembly elements of the 30S small ribosomal subunit. These observations suggest direct involvement of Era in the functional assembly of the 30S small ribosomal subunit of *E. coli* (20).

In eukaryote, depletion and mutation of ERA, a chicken homologue of Era, in chicken DT40 cells led to growth impairment, accompanied by an accumulation of apoptotic cells (21,22), suggesting that ERA also plays an essential role in eukaryotic cells. The chicken ERA protein regulates the G1 phase progression via an as yet unknown molecular mechanism, in which an RNA recognition domain of ERA protein was shown to be important. However, there are no investigations on its subcellular localization and function at mitochondria in DT40 cells.

We have previously found that ERAL1, a human orthologue of ERA, is associated with mitochondrial TFAM protein (17). ERAL1 has a putative N-terminal mitochondria targeting sequence of 59 amino acids. Here, we first show that ERAL1 is localized in the mitochondrial matrix. Then, we sought to figure out the roles of human ERAL1 in mitochondrial functions. We have examined what mitochondrial components are associated with ERAL1 protein. To know the physiological roles of ERAL1 in mitochondria, we have investigated the mitochondrial functions such as mitochondrial membrane potential and reactive oxygen species (ROSs) production after siRNA-mediated knockdown of ERAL1. Furthermore, we provide evidence that ERAL1 is required for proper assembly of mitochondrial ribosomal subunits and thus important for mitochondrial translation. Interestingly, the siRNA knockdown of ERAL1 led to cell growth retardation. These results suggest that mitochondrial ribosome-associated ERAL1 plays an important role in mitochondrial function as well as viability of human cells.

METHODS

Antibody

Anti-hemagglutinin (Anti-HA), TFAM, endonuclease G (EndoG), mitochondrial single-stranded binding protein (mtSSB), leucin rich protein 130 (LRP130), elongation factor-Tu (EF-Tu), ERAL1 were raised in our own laboratory. Anti-Calnexin, Histon H1, BAP37 were purchased from StressGen (AnnArber, MI, USA), Millipore (Millerica, MA, USA) and SantaCruze (SantaCruze, CA, USA), respectively. MitoTracker Red and H_2DCFDA were purchased from Invitrogen (Carlsbad, CA, USA).

Cell culture

Human cervical cancer HeLa cells were cultured in Dulbecco Eagle's minimal essential medium (Sigma, St Louis, MO, USA) with 10% heat-inactivated fetal bovine serum (FBS). Cell lines were maintained in a 5% CO_2 atmosphere at 37°C. In some experiments, glucose-free Dulbecco's modified eagle medium was supplemented with 0.9 mg/ml galactose, 1 mM sodium pyruvate, 10% FBS and 2 mM L-glutamine.

Immunofluorescent imaging of HeLa cells

Human HeLa cells were incubated in the presence of 100 nM MitoTracker Red for 20 min. After washing with phosphate-buffered saline (PBS) three times, the cells were fixed with 3.7% formaldehyde for 30 min, then incubated with PBS containing 0.1% Triton X-100 for 30 min. After washing with PBS three times, the fixed cells were blocked with PBS containing 1% bovine serum albumin (BSA) for 30 min. Then the cells were incubated with 250-fold diluted anti-HA or -TFAM antibody in PBS/BSA for 1 h. After washing the cells with wash buffer (PBS containing 0.1% Tween-20) three times, the cells were incubated with 250-fold diluted Alexa Fluor 488 goat anti-rabbit IgG (Invitrogen) for 30 min. The glass slides were mounted using Slowfade mounting medium (Invitrogen). Fluorescence images were obtained under a confocal laser microscope (Nikon, Tokyo, Japan).

Immunoblot analysis

HeLa cells were lysed with Lysis buffer (50 mM Tris–HCl, pH 7.5, 1 mM EDTA, 150 mM NaCl and 0.5% NP-40) (TNE) and total lysate (20 μg) were subjected to immunoblot analysis as described previously (23) using polyclonal antibodies or monoclonal antibodies against COX II (Invitrogen), caspase 3, cleaved caspase 3 (Cell signaling, Danvers, MA, USA) and death associated protein 3 (DAP3) (SantaCruz).

Proteins (20 μg) were separated by SDS–polyacrylamide gel electrophoresis (SDS–PAGE) and immunoblotted with indicated specific antibodies. The signals were visualized with horseradish peroxidase-labelled anti-rabbit immunoglobulin G and an ECL reagent (GE healthcare). The chemiluminescence was recorded and quantified with a chilled charge-coupled device camera, LAS1000plus (Fuji Photo Film, Tokyo, Japan).

Knockdown analysis using siRNAs

The following double-stranded ERAL1 RNA 25 bp oligonucleotides were generated from Stealth Select RNAi (Invitrogen): 5′-UAACCAUAGCAACAGAGUGCGUUCC-3′ and 5′-GGAACGCACUCUGUUGCUAUGGUUA-3′. siRNA transfections were performed according to

the manufacturer's instructions (Invitrogen). Briefly, 2 μl Oligofectamine (Invitrogen) was diluted in 100 μl Opti-MEM I medium (Invitrogen) and incubated for 5 min at room temperature. Next, 20 pmol ERAL1 or control duplex Stealth RNA (Invitrogen) in 100 μl Opti-MEM I were added gently and incubated for 20 min at room temperature. Oligomer-Oligofectactamine complexes and aliquots of 2×10^5 HeLa cells in 2 ml culture medium were combined and incubated for 10 min at room temperature. The cells were seeded in six-well dishes with 2 ml culture medium and assayed at indicated time for western blotting and FACS analysis.

Cell proliferation assay

To determine cell proliferation, HeLa cells transfected with control- or ERAL1-siRNA were seeded in 24-well plates at a density of 2×10^4 cells per well. After 24 h, one set of cells was trypsinized, resuspended in PBS and counted by a cell counter (Beckman Coulter, Fullerton, CA, USA) (24). Cells were counted in a similar way every 24 h, up to 96 h.

Expression of ERAL1 in HeLa Tet-on cells

cDNA of ERAL1 containing the deduced first methionine site was amplified from a cDNA library of human HeLa cells by polymerase chain reaction (PCR) using a primer set: 5′-AT GGC TGC CCC CAG CTG GCG and 5′-TCA CTT GAG GAG CTT CAC AGA GAG. Then BamHI and SpeI sites were added to the 5′- and 3′-terminals, respectively, of the cDNA by a second PCR using primers, 5′-ATA TGG ATC CAT GGC TGC CCC CAG CTG GCG and 50-ATATACTAGT CTT GAG GAG CTT CAC AGA GAG. The PCR product was digested with BamHI and SpeI. The DNA fragment encoding ERAL1, a DNA fragment encoding an HA-tag, and a pcDNA5/FRT vector (Invitrogen) were digested with BamHI and NheI and then were ligated. The vector was named pERAL1-HA. We transfected HeLa/FRP/Tet-on cells with the pERAL1-HA vector and selected cells bearing the transgene in the presence of hygromycin B (200 μg/ml) as previously described (25).

Submitochondrial localization

HeLa cells (1×10^8 cells) cultured in 10-cm dishes were scraped off with a cell lifter, suspended in PBS, precipitated by centrifugation and washed with homogenizing buffer (10 mM HEPES-KOH, pH 7.4, 0.25 M sucrose and 1 mM EDTA). The cells were then suspended in four volumes of the same buffer, homogenized with a Potter-Elvehjem homogenizer, and centrifuged at 900*g* for 10 min. The supernatant was centrifuged at 10 000*g* for 6 min. The pellet was collected as a crude mitochondrial fraction. The crude mitochondria (20 μg) were suspended in hypotonic buffer (10 mM HEPES-KOH, pH 7.4 and 1 mM EDTA) at 4°C for disruption of the mitochondrial outer membranes. After the hypotonic treatment, the mitochondria were precipitated by centrifugation at 10 000*g* for 6 min. The mitochondria were resuspended in hypotonic buffer and then digested with proteinase K (200 μg/ml) with or without 1% Triton X-100 on ice for 20 min. The protein was precipitated by the addition of 15% trichloroacetic acid. The precipitates were solubilized in sample buffer (6% SDS, 150 mM Tris base, 10 mM EDTA and 25% glycerol), separated by SDS–PAGE, and analysed by immunoblotting.

Immunoprecipitation using anti-HA antibodies

Each step was done at 4°C or on ice. Doxycyclin-induced HeLa (ERAL1-HA) cells (1×10^8 cells) were homogenized with a Potter-Elvehjem homogenizer in 2 ml of homogenizing buffer (10 mM HEPES-KOH, pH 7.4, 0.25 M sucrose and 1 mM EDTA) and centrifuged at 900*g* for 10 min. The supernatant (~2 ml) was diluted with 2 ml of 20% Percoll buffer [0.25 M sucrose, 20 mM Tris-HCl, pH 7.4, 1 mM EDTA and 20% Percoll (GE healthcare)], and the sample was overlaid on a discontinuous Percoll density gradient (4 ml of 40% and 4 ml of 20% Percoll buffer) in a 12-ml centrifugation tube. After centrifugation at 24 000 r.p.m. for 1 h using a SW41Ti rotor (Beckman Coulter), a mitochondrial band located in the middle of the tube was taken. Two to three milligrams of mitochondrial protein were solubilized in 1 ml of IP buffer (10 mM Tris–HCl, pH 7.4, 150 mM NaCl, 1 mM EDTA, 0.5% BSA and 0.5% NP-40) containing 40 μl of beads coated with anti-HA antibodies and control mouse IgG. After 12 h rotation, the beads were washed four times with wash buffer (IP buffer without BSA) and eluted with 1 M glycine (pH 2).

Immunoprecipitation after crosslinking

All procedures were done at 4°C or on ice. Two milligrams of mitochondrial protein were suspended in 1 ml of crosslinking buffer (0.25 M sucrose, 20 mM HEPES–KOH, pH 7.4, 2 mM EDTA and 25 mM NaCl). Then 27 μl of 37% formaldehyde or distilled water (as a control) were added and the mixture was kept on ice for 2 h. After incubation, 125 μl of 1M glycine was added to quench the crosslinking reaction, and the sample was centrifuged at 10 000*g* for 1 min to precipitate the mitochondria. The mitochondria were solubilized with 100 μl of IP buffer containing 1% SDS. After 10-fold dilution with 1 ml of IP buffer, the immunoprecipitation reaction was done as described above. The immunoprecipitates were heated at 95°C for 30 min to cleave the crosslinks and the proteins were separated by 12% SDS–PAGE. Bands were visualized by staining with Coomassie Brilliant Blue (CBB). The immunoprecipitates were separated by SDS–PAGE and immunoblotted with each antibody.

In-gel protein digestion and LC-MS/MS

A CBB-stained band was excised and the protein was digested with Lysyl Endopeptidase (WAKO, Japan) in digestion buffer (100 mM Tris–HCl, pH 9.0, 0.5% SDS and 1 mM EDTA) for 12 h. The supernatant containing the digested peptides was analysed by liquid chromatography and mass spectrometry (LC/MS/MS) (Agilent 1100 Series an LC/MS system). The peptide masses were assigned to the peptide mass databases using the MASCOT program (MATRIX SCIENCE). All proteins in the SWISS-PROT

mammalian database were taken into account. The peptide mass error was limited to 1.0 Da and the MS/MS mass error was limited to 0.8 Da. Only one missed cleavage was accepted.

Analysis of ROS production

The intracellular H_2O_2 concentration was estimated by means of an oxidation-sensitive fluorescent probe dye, 2′7′-dichlorodihydrofluorescein diacetate (H_2DCFDA) (Invitrogen). H_2DCFDA was deacetylated intracellularly by non-specific esterase, which was further oxidized by cellular peroxides to the fluorescent compound, 2,7-dichlorofluorescein (DCF). In brief, cells were incubated with the ERAL1- or control siRNA for 72 h. The cells were then washed in PBS and incubated with 20 μM H_2DCFDA at 37°C for 30 min according to the instructions of the manufacturer. DCF fluorescence was detected using a fluorescence activated cell sorting (FACS) caliber flow cytometry (Becton Dickinson, Flanklin Lakes, NJ, USA). For each sample, 10 000 events were collected. H_2O_2 production was expressed as mean fluorescence intensity, which was calculated by FlowJo software.

Pulse-labelling of mitochondrial translation products

In vitro pulse-labelling of mitochondrial translation with [^{35}S]-(methionine and cysteine) (GE Healthcare) for 1 h was performed. In experiments where the label was chased, cells were incubated for 6 min in emetine (100 μg/ml) prior to labelling. The labelled cells were rinsed with isotonic buffer (25 mM Tris–HCl, pH 7.4, 137 mM NaCl, 10 mM KCl, 0.7 mM Na_2HPO_4). After centrifuge 115*g* for 5 min, the pellets were suspended in loading buffer containing 93 mM Tris–HCl, pH 6.7, 7.5% glyrerol, 1% SDS, 0.25 mg/ml of bromophenol blue and 3% mercaptoethanol. And the total lysate (50 μg) was loaded and run on 14% SDS–PAGE for 3 h at 180 V. The gels were fixed in a methanol–acetic acid solution, treated with Amplify and measured by BAS2500 (Fuji).

Sucrose gradient analysis of mitochondrial ribosomes

Cell lysates were prepared from HeLa cells treated with ERAL1 or non-targeted (Control) siRNA for 72 h. The HeLa cells were solubilized in a non-ionic detergent (1% lauryl maltoside). Total cell lysates (2 mg) were loaded on a 10–35% sucrose density gradient in 10 mM Tris–HCl, pH 7.2, 150 mM NaCl, 1 mM EDTA and centrifuged for 3 h at 100 000*g* at 4°C by using a swinging bucket SW 40.1 rotor (Beckman Coulter). After separation through 10–35% sucrose gradients, fractions were precipitated by 10% trichloroacetic acid and washed in acetone, and the entire fraction was resolved by SDS–PAGE. The small (Elongation Factor-Tu(EF-Tu) DAP3, MRPS22) and large (MRPL3) mitochondrial ribosomal subunits, ERAL1, cytochrome c oxidase (COX) II, TFAM, Lon and LRP130 were detected by immunoblotting. For real time PCR, RNA was extracted from 50 μl of fractions and was assayed by real time PCR.

To co-immunoprecipitate RNA with ERAL1-HA protein

We used a previously described procedure (24). Briefly, HeLa mitochondria lysates induced by doxycycline were first pre-cleared with 50 μg of rabbit IgG (Bio-Rad) by bath-sonicating for 15 min at 4°C, followed by binding to anti-HA agarose beads and control IgG for 12 h at 4°C. The complexes were pulled down and washed four times with 1 ml of immunoprecipitation buffer. Then, RNA was eluted from the beads with a QIAGEN RNAeasy kit (QIAGEN, Hilden, Germany). Two micrograms of the eluted mitochondrial RNA (mtRNA) were treated by DNase I (100 units) at 37°C for 30 min and then the mtRNA was cleaned with an RNAeasy kit. The RNA pellets were resuspended in water and stored at −70°C.

Quantification of mRNAs

Total RNA was extracted from HeLa cells or a fraction of sucrose density gradient with a QIAGEN RNAeasy kit (QIAGEN). Two micrograms of RNA were treated by DNase I (100 U) at 37°C for 30 min and then RNA was cleaned with an RNAeasy kit. The reverse transcription (RT) of 1 μg of the total RNA was performed with SuperScript II RT (Invitrogen) according to manufacturer's instructions. Random 6-mer primers were used in the RT reaction. The expressions of mitochondrial genes were detected by quantitative PCR with a thermal cycler (StepOne plus, Invitogen). The PCR primers were listed in Supplementary Table S1.

RT-PCR

RT reactions were carried out using SuperScript II RT and random primers in a 20 : 1 volume following the manufacturer's protocol. RT reaction mixtures were diluted 1 : 10 with water and the cDNAs were used for PCR. Primer pairs were shown in supplementary Data.

RESULTS

ERAL1 in mitochondria

ERAL1 is a protein composed of 368 amino acids as deduced from its cDNA. The existence of a 59-amino acid N-terminal mitochondria targeting sequence was predicted by MitoProt II, a prediction program for mitochondrial localization. The probability of mitochondrial localization is 0.9998 for ERAL1. Then, we produced stable cell lines that express the recombinant full length ERAL1 with a C-terminal HA tag (ERAL1-HA) upon induction by doxycycline addition. The recombinant ERAL1-HA was seen only after the induction by doxycycline-addition at 24 and 48 h (Figure 1A). In immunocytochemistry, the ERAL1-HA was granularly stained with anti-HA antibodies after the induction (Figure 1B). The HA-staining is completely co-localized with the mitochondria visualized with a MitoTracker Red dye, suggesting that the expressed ERAL1 is exclusively localized at mitochondria.

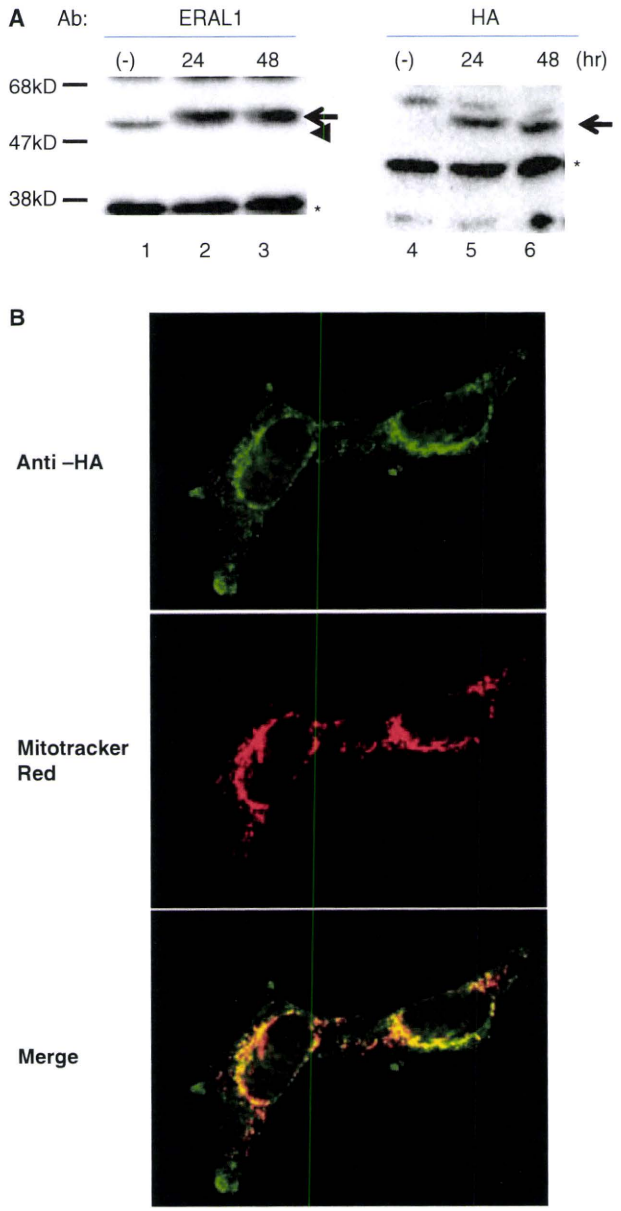

Figure 1. Inducible expression of recombinant ERAL1 with an HA tag. (**A**) ERAL1 with an HA tag was inducibly expressed in HeLa cells using a Tet-on system as described under 'Methods' section. ERAL1 was detected by immunoblotting with anti-ERAL1 (lanes 1–3) and anti-HA (lanes 4–6) antibodies. Lanes 1/4; no induction, lanes 2/5 and 3/6; 24 and 48 h after tetracycline treatment, respectively. Arrows and an arrowhead indicate recombinant and endogenous ERAL1, respectively. Asterisks show non-specific bands. (**B**) Immunocytochemistry of recombinant ERAL1. The ERAL1-HA-transfected cells were cultured in the presence of doxycyclin for 48 h. Mitochondria and the recombinant ERAL1 were visualized with a mitochondria-staining dye, MitoTracker Red, (middle panels) and anti-HA antibodies (upper panel), respectively. The lower panels are merged.

Subcellular localization of ERAL1

Then we examined the intracellular localization of ERAL1 by cellular fractionation. The HeLa cells were separated into Nuclear (Nu), Mitochondrial (Mt), microsomal (Micro) and cytosolic (Cyt) fractions. Calnexin, histoneH1, mtSSB and TFAM were detected by immunoblotting as markers for endoplasmic reticulum, nuclei, mitochondria and mitochondria, respectively. The mitochondrial fraction contained essentially no histoneH1, a nuclear protein, indicating minimal contamination of the mitochondrial fraction by nuclei (Supplementary Figure S1). ERAL1-HA was found mostly in the mitochondrial fraction as were TFAM and mtSSB (Supplementary Figure S1, third lane). TFAM was also very weakly detected in the nuclear fraction. Calnexin was detected in the microsomal fraction. These results suggest again that ERAL1 is localized at mitochondria.

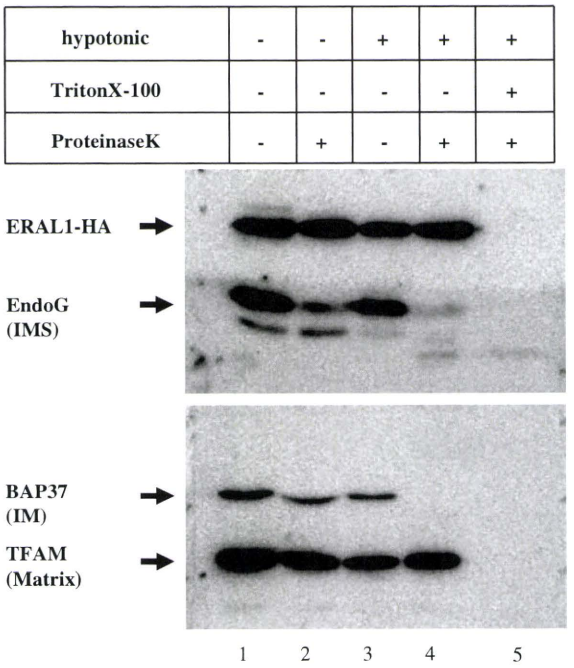

Figure 2. Submitochondrial localization of exogenous ERAL1-HA. Mitochondria were incubated in hypotonic buffer for disruption of the outer membranes without (lanes 3 and 4) or with a non-ionic detergent, Triton X-100 (lane 5). Then the mitochondria were digested with proteinase K (lanes 2, 4 and 5). The indicated proteins were detected by immunoblotting. EndoG, BAP37 and TFAM are markers for the mitochondrial IMS, IM and matrix, respectively.

Submitochondrial localization of ERAL1

Next we examined the submitochondrial localization of ERAL1-HA. The mitochondrial outer membranes were disrupted by hypotonic treatment (Figure 2, lanes 3 and 4) as verified by the observation that EndoG is localized in the intermembrane space (IMS), was completely digested by proteinase K (Figure2, lane 4). BAP37, which is an inner membrane (IM) protein and largely faces the IMS, was digested by proteinase K. On the other hand, TFAM, which localizes in the matrix, was resistant to the proteinase K digestion (Figure 2, lane 4 in lower panel), indicating that the IMs were intact. Under these hypotonic conditions, ERAL1 was not cleaved by proteinase K (Figure 2, lane 4 in upper panel). When the IMs were solubilized with a non-ionic detergent Triton

X-100, both TFAM and ERAL1 were cleaved by proteinase K (Figure 2, lane 5). Taken together, these results suggest that ERAL1 is localized in the mitochondrial matrix side of IM.

RNA immunoprecipitation

Escherichia coli Era protein has the KH domain which can bind to RNA. We performed RNA immunoprecipitation assay to test whether ERAL1 protein associates with mitochondrial ribosome including the mitochondrial ribosome RNA or mitochondrial transcripts *in vivo*. Mitochondrial lysates were prepared using immunoprecipitation buffer. After immunoprecipitation with anti-HA antibodies, RNA was extracted from the immunoprecipitates and the eluted mtRNA was used as a template in the RT reaction (Figure 3A). As a control, total mtRNA was used in the RT reaction (Figure 3A, lane 5). First, primer pairs covering 12S rRNA were used in the PCR. A PCR product with a predicted size was obtained for 12S mitochondrial rRNA from the mtRNA (Figure 3A, lane5) and the mtRNA obtained from the HA-immunoprecipitates (Figure 3A, lane 4). There were no PCR products irrespective of the RT reaction when the template was obtained by immunoprecipitation with control IgG (Figure 3A, lanes 1 and 2). There were also no PCR products without RT from the HA-immunoprecipitates (Figure 3A, lane 3), indicating no DNA contamination. Next we investigated whether ERAL1 protein was associated with the other mitochondrial transcripts. We examined 16 PCR primer sets for mitochondrial genes. Only 12S ribosomal RNA was PCR-amplified (Figure 3B). These results suggest that ERAL1 is associated with the mitochondrial ribosomal small subunit which contained 12S mitochondrial ribosomal RNA or directly associated with 12S rRNA. The latter is likely based on its homology to bacterial Era and chicken ERA.

Proteins associated with ERAL1

To seek for proteins interacting with ERAL1 in mitochondria, we immunoprecipitated ERAL1-HA-associated proteins with anti-HA antibodies after cross-linking reactions (Figure 4, upper panel). Under these conditions, DAP3 (mitochondrial ribosome protein S29), LRP130 and EF-Tu (mitochondrial translation elongation factor) were detected in the immunoprecipitates

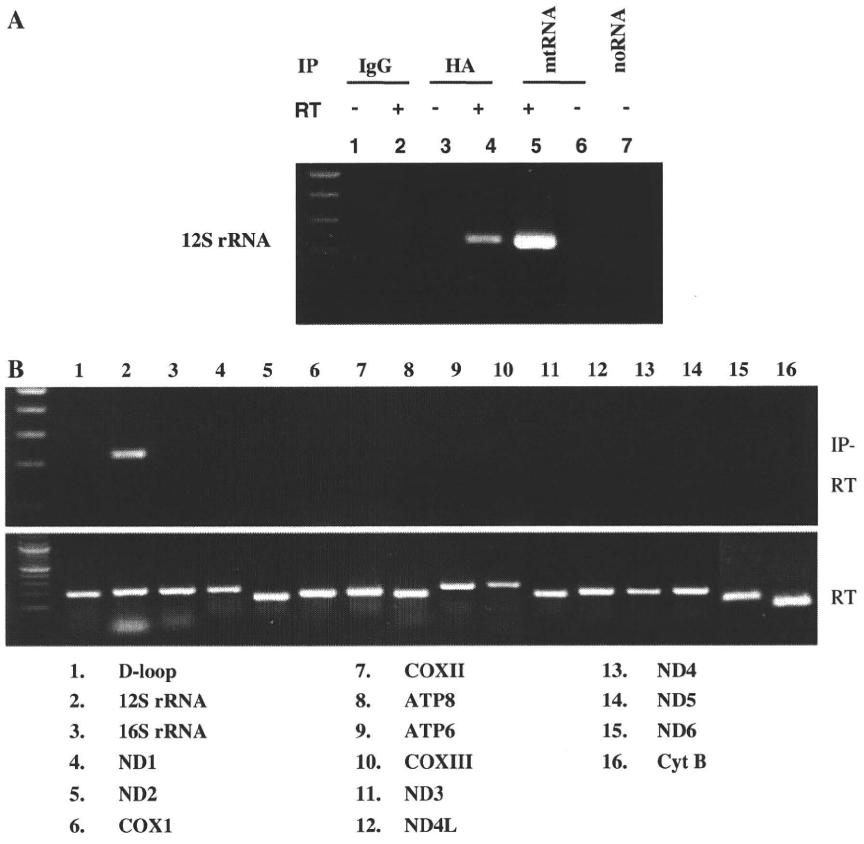

Figure 3. ERAL1 is associated with mitochondrial 12S rRNA in HeLa cells. (**A**) ERAL1-HA-transfected HeLa cells were treated by tetracycline for 48 h. The cells were lysed by TNE buffer and immunoprecipitated with control IgG (lanes 1 and 2) or anti-HA antibodies (lanes 3 and 4). RNAs were extracted using an RNAeasy kit from the immunoprecipitates (lanes 1–4) and whole cells (lanes 5 and 6) and then treated with DNaseI. The DNaseI-treated RNAs were subjected to RT (lanes 2, 4 and 5) or not subjected to RT (lanes 1, 3 and 6) and then amplified by PCR with a primer set for 12S rRNA. No RNA template in lane 7. (**B**) The RNA in lane 4 of (A) (IP-RT, upper panel) and that in lane 5 of (A) (RT, lower panel) were amplified similarly by PCR using indicated primer sets for 16 mitochondrial genes.

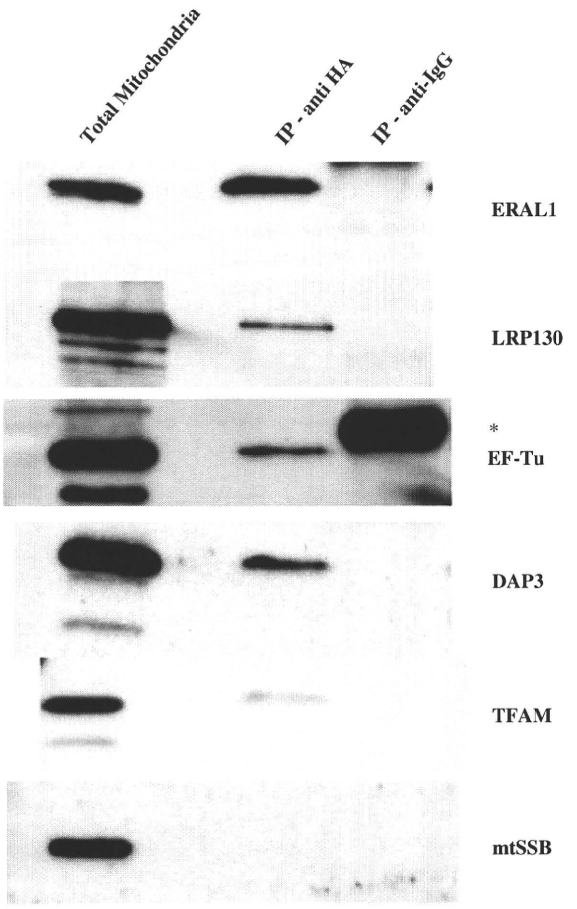

Figure 4. Mitochondrial proteins crosslinked to ERAL1-HA. ERAL1-HA-transfected HeLa cells were treated by tetracycline for 48 h. Mitochondrial fraction was purified by percoll density gradient and lysed by TNE buffer. Immunoprecipitates obtained with anti-HA and mouse-IgG were separated by SDS–PAGE and then immunoblotted with anti-EF-Tu, ERAL1, LRP130, TFAM, mtSSB and DAP3 antibodies. An asterisk indicates a heavy chain of IgG.

(Figure 4), suggesting that ERAL1 is located close to mitoribosome or translation related machinery. We also detected TFAM in the immunoprecipitates.

The other cross-linked proteins which were found by LC-MS/MS analysis are listed in Table 1. The LC-MS/MS analysis revealed three mitoribosomal proteins, presumably indicating the presence of ERAL1 in the small (28S) ribosomal subunits. The second group was proteins which were reported to be associated with human mitochondrial nucleoids. There were factors involved in intra-organellar translation, nucleic acid binding proteins and chaperones/proteases, all of which are expected to associate with ribosomal components or nascent peptides. Several polypeptides known to be involved in metabolism were also identified. In non-cross-linked experiments, we observed that ERAL1 was associated with two tRNA synthetase and Stress70 protein. In summary, many proteins related to chaperons and translation machinery were identified by LC-MS/MS.

siRNA-mediated knockdown of ERAL1 induced mitochondrial dysfunction

To identify the ERAL1 function in mitochondria matrix, we used an siRNA strategy to downregulate the ERAL1 expression. Because ERAL1 localized in mitochondrial matrix and associated with mitochondrial ribosomes, we hypothesized that suppression of the ERAL1 expression could have an impact on mitochondrial function, especially translation. The expression of ERAL1 was diminished by ERAL1-targeted siRNA treatment for 72 h. However, DAP3, cytochrome *c* and TFAM were not affected by the ERAL1 knockdown for 72 h (Figure 5A). A non-targeting siRNA (control siRNA) was used to confirm specificity.

Reduced translation rate *in vivo* labelling

To investigate the defect in mitochondrial protein synthesis caused by the ERAL1 siRNA transfection, HeLa cells were pulse-labelled with a mixture of [^{35}S] methionine and [^{35}S] cystein in the presence of emetine, an inhibitor of cytoplasmic translation. The overall rate of protein synthesis in mitochondria of the ERAL1 siRNA transfectants was ~50% of the control siRNA transfectants as shown in Figure 5B. Especially, the protein synthesis rate of COX I, II and III seemed more strongly decreased than the other proteins when ERAL1 was downregulated. These results suggest that ERAL1 protein is involved in mitochondrial translation.

Depletion of ERAL1 decreased COX II protein

To verify the selective effects on the protein synthesis by the ERAL1 knockdown, HeLa cells were transfected with the ERAL1 siRNA and the changes of several proteins were analysed by western blotting. ERAL1 protein was decreased by 24 h after the ERAL1 siRNA transfection. mtSSB was not altered up to 96 h (Figure 5C). Consistent with the stronger decrease of the COX II translation (Figure 5B), a COX II protein level was decreased at 48 h after the siRNA transfection (Figure 5C).

Next, to see if the overall decrease of the mitochondrial translation was affected by the amounts of mRNAs, we investigated effects of the ERAL1 depletion on expression of the mitochondrially encoded RNAs. The ERAL1-directed siRNA significantly lowered the mRNA levels of 12S rRNA, COX I, COX II and ND5 (Figure 5D), but at most moderately affected the 16S rRNA, ND1, ND2, ND3, ND4, cyt b and ND4L transcripts. This relatively stronger decrease of COX II mRNA might contribute in part to the apparent stronger decrease of the COX II translation. The decrease of 12S rRNA might be caused by disassembly of the mitoribosomes as shown later (Figure 6A). It is currently unknown how the other mRNAs was decreased by the ERAL1 depletion.

Depletion of ERAL1 affects mitochondrial small subunit

The ERAL1 siRNA inhibited the mitochondrial protein synthesis. To further clarify a role of ERAL1 in the mitochondrial translation, we analysed sedimentation profiles in a sucrose density gradient (Figure 6A). The 3-days

Table 1. List of proteins identified in complex with ERAL1

Swiss-Prot accession number	Gene symbol	Name	No. of peptides matched	% Sequence coverage	MW	PI	Nucleoid type
P38646	HSPA9	Stress-70 protein	8	17	73920	5.87	Class I
Q15031	LARS2	Leucyl-tRNA synthetase	4	4	102823	8.46	
Q9BW92	TARS2	Threonyl-tRNA synthetase	1	1	81841	6.9	
P31327	CPS1	Carbamoyl-phosphate synthase	8	4	165975	6.30	Class I
P42704	LRPPRC	Leucine-rich PPR motif-containing protein	7	5	159003	5.81	Class I
Q00059	TFAM	Transcription factor A	1	4	29306	9.74	Class I
P34897	SHMT2	Serine hydroxymethyltransferase	3	5	56414	8.76	Class I
P49411	TUFM	Elongation factor Tu	3	8	49852	7.26	Class I
P10809	HSPD1	60 kDa heat shock protein	24	37	61187	5.70	Class II
Q99623	PHB2	Prohibitin-2	7	24	33276	9.83	Class II
P40926	MDH2	Malate dehydrogenase	2	7	35965	8.92	Class III
P54886	ALDH18A1	Delta-1-pyrroline-5-carboxylate synthetase	3	3	87989	6.66	
Q12931	TRAP1	Heat shock protein 75 kDa	3	4	80345	8.30	
P31040	SDHA	Succinate dehydrogenase [ubiquinone] flavoprotein subunit	1	2	73672	7.06	
Q5R1W8	VIM	Vimentin	6	17	53677	5.03	
P00367	GLUD1	Glutamate dehydrogenase 1	6	12	61701	7.66	
P55084	HADHB	Trifunctional enzyme subunit γ	1	2	51547	9.45	
O75616	ERAL1	GTP-binding protein era homologue	20	32	48833	9.05	
P60709	ACTB	Actin, cytoplasmic 1	5	15	42052	5.29	
P82650	MRPS22	28S ribosomal protein S22	1	3	41425	7.70	
P04406	GAPDH	Glyceraldehyde-3-phosphate dehydrogenase	3	12	36201	8.57	
P48047	ATP5O	ATP synthase subunit O	4	24	23377	9.97	
Q9UIK4	DAPK2	Death-associated protein kinase 2	2	4	43042	6.45	
Q92665	MRPS31	28S ribosomal protein S31	2	6	45405	9.32	
Q46199	MTIF2	Translation initiation factor IF-2	3	2	81837	6.71	
P82909	MRPS36	28S ribosomal protein S36	1	4	11459	9.99	

The columns correspond to their accession number, gene symbol, name, number of unique peptide matched, percent sequence coverage, estimated MW and PI identified by LC-MS/MS analysis. We observed top three proteins in non-crosslinkng condition. Putative nucleoid proteins as recently classified by Bogenhagen *et al.* (29). Class I: core nucleoid protein, Class II: proteins seen in native but not cross-linked nucleoids and Class III: proteins seen in cross-linked but not native nucleoids.

treatment with the ERAL1 siRNA significantly decreased ERAL1 in a HeLa cell (Figure 6A, panels 1 and 2) as well as COX II (Figure 6A, panels 9 and 10) as expected. Either the amounts or distribution profiles of the other proteins were not changed by the ERAL1 depletion (Figure 6B). Therefore, the same number of fraction may be comparable before and after the ERAL1 depletion.

ERAL1 largely co-migrated with the small ribosomal subunit proteins (MRPS22 and DAP3) (Figure 6A, panels 1, 3 and 5), suggesting that ERAL1 associates with the small subunit of mitochondrial ribosome (Figure 6A). The treatment caused a striking change in the distribution of MRPS22, proteins of the small ribosomal subunits. In spite of the decrease of overall amount, MRPS22 became evident also in fractions 11 and 12 (Figure 6A, compare panels 3 and 4). Thus, the ERAL1 siRNA treatment shifted the distribution of MRPS22 to heavier fractions. These results suggested that ERAL1 is required for proper assembly of mitochondrial ribosomal small subunits. Conversely, MRPL3 protein were distributed within fractions 9–11 (Figure 6A, panels 7 and 8) and the distribution of MRPL3 were barely changed by the ERAL1 depletion. Taken together, we consider that the ERAL1 associates with small ribosomal subunit and ERAL1 depletion compromises assembly of the small ribosomal subunit.

Next, we investigated the sedimentation profile of 12S rRNA (small subunit) and 16S rRNA (large subunit) in the sucrose density gradient (Figure 6C and D). Quantitative PCR analysis showed that the amount of 12S rRNA at fraction 7–8 was decreased after ERAL1 depletion. However, the abundance of 12S rRNA at fractions 9–10 was not changed even after the ERAL1 depletion (Figure 6C). The relative 12S rRNA distribution is consistent with the results of MRPS22 protein (Figure 6A and C). The distribution and the total amount of 16S rRNA were little changed even after the ERAL1 depletion, suggesting that the ERAL1 depletion did not affect the assembly of the large subunit itself (Figure 6D). Taken together, we consider that the ERAL1 depletion affected assembly of the small ribosomal subunit.

ERAL1 siRNA-mediated knockdown reduced MMP

The ERAL1 siRNA-mediated inhibition of the mitochondrial translation may influence mitochondrial functions. First, we measured mitochondrial membrane potential (MMP) ($\Delta\psi m$) using JC-1 that is a fluorescent dye sensitive to mitochondrial membrane potential. The $\Delta\psi m$ value of ERAL1 siRNA transfectants was lower than those of normal as well as control siRNA transfected cells (Supplementary Figure S3). carbonyl cyanide m-chlorophenylhydrazone (CCCP)-treated cells served as a positive control for depolarization of the mitochondrial membrane.

The lower mitochondrial membrane potential in the ERAL1 siRNA-transfected cells was further confirmed by staining with MitoTracker Red, a fluorescent dye

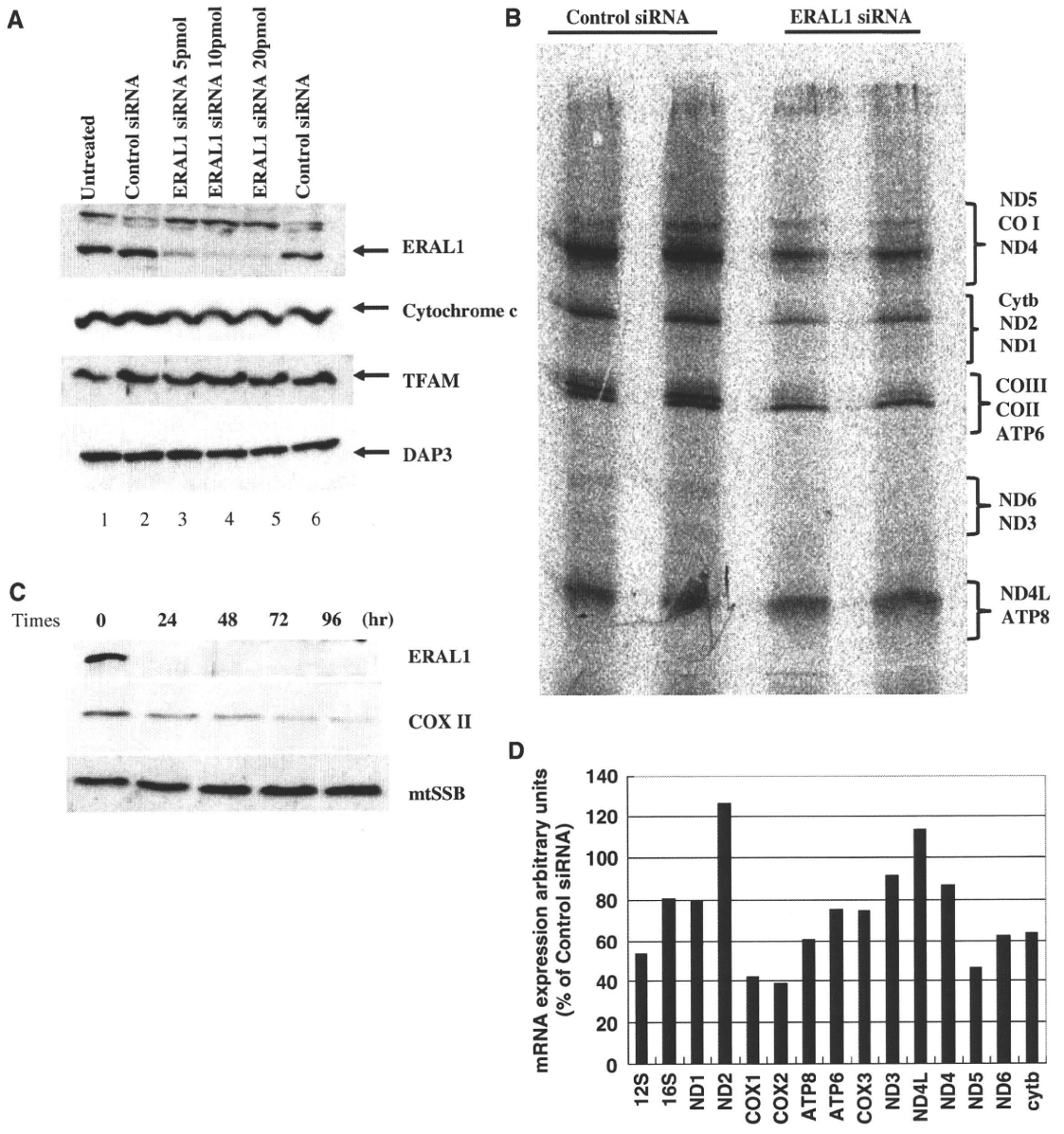

Figure 5. siRNA-mediated knockdown of ERAL1 and *in vivo* labelling. (**A**) HeLa cells were transfected with nothing (lane 1), control siRNA (lanes 2 and 6), and 5, 10, 20 pmol of ERAL1 siRNA (lanes 3–5) using oligofectamine. After 2 days of the transfection, the cells were lysed and followed by immunoblotting with anti-ERAL1, cytochrome *c*, TFAM and DAP3 antibodies. (**B**) Synthesis of mitochondrial polypeptides. HeLa cells were transfected with control and ERAL1 siRNAs for 72 h. These cells were pulse-labelled in the presence of emetine. The mitochondrial translation products were run on a 15–20% polyacrylamide gradient gel. The gel was processed for fluorography as detailed in the 'Methods' section. The seven complex I subunits (ND), one complex III subunit (cyt b), three complex IV subunits (COX) and two complex V subunits (ATP) are indicated on the right. (**C**) siRNA-mediated knockdown of ERAL1. HeLa cells were transfected with ERAL1 siRNA and harvested every 24 h. The cells were lysed and followed by immunoblotting with anti-ERAL1, COX II and mtSSB antibodies. (**D**) Quantification of mitochondria-encoded mRNA. HeLa cells were treated with control or ERAL1 siRNA for 72 h. The amounts of mRNAs were measured as described under 'Methods' section. The value in control siRNA-treated cells is 100% for each mRNA.

accumulating in mitochondria depending on the mitochondrial membrane potential. HeLa cells were transfected with control and ERAL1 siRNAs for 72 h. The cells pre-treated with MitoTracker Red for 20 min were fixed and then TFAM was stained with anti-TFAM antibodies (Supplementary Figure S4). The fluorescence intensity or pattern of TFAM staining was not changed (upper panel), however the ERAL1 siRNA-mediated knockdown cell were significantly weakly stained with MitoTracker Red (center and lower panels, right), suggesting that the ERAL1 depletion reduced the mitochondrial membrane potential.

Depletion of ERAL1 increases mitochondrial ROS

Stress conditions in mitochondria are frequently associated with elevated levels of ROS. A tight link exists between mitochondrial ROS generation and

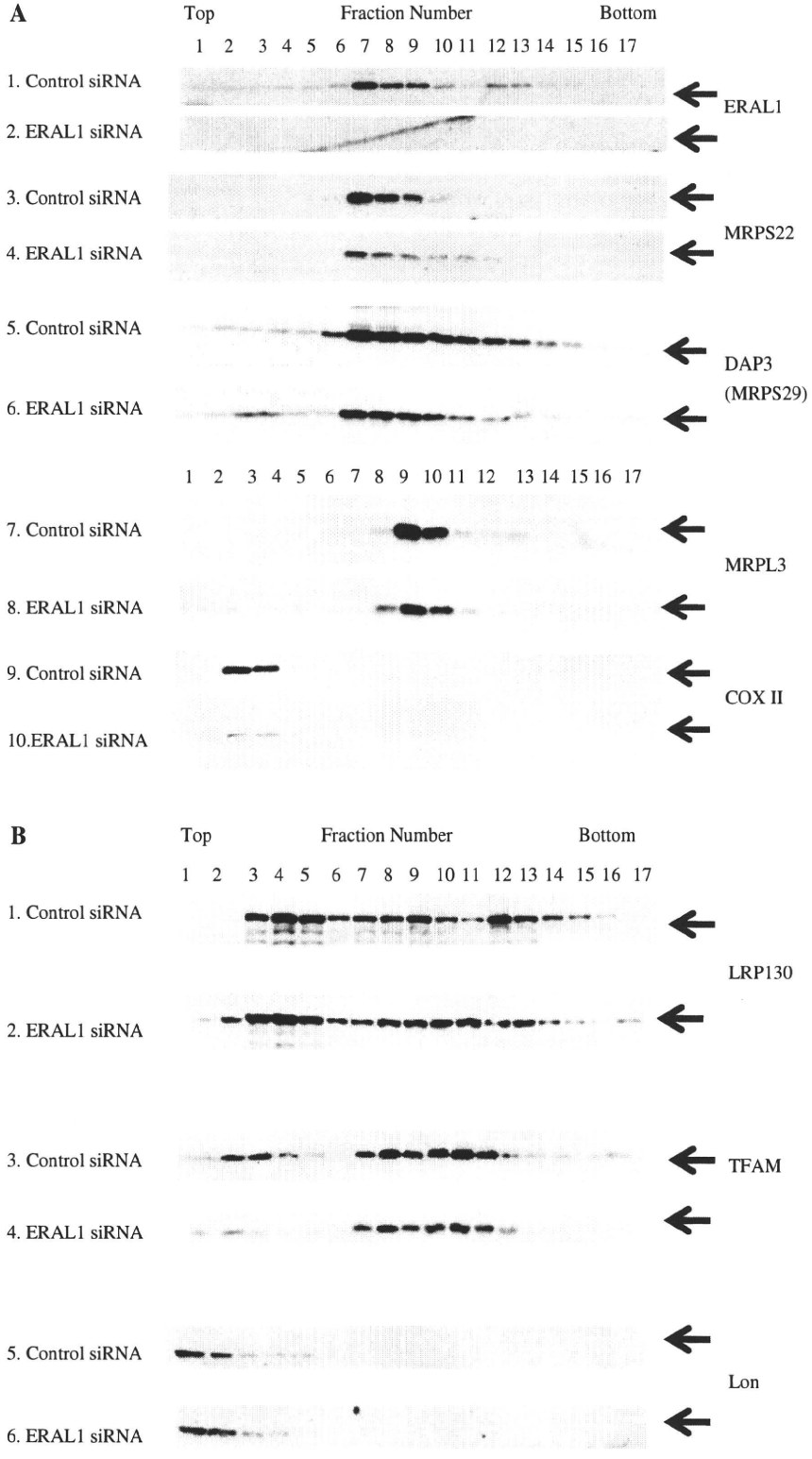

Figure 6. Reduction of ERAL1 results in redistribution of ribosomal protein and ribosomal RNA. (**A** and **B**) Cell lysates were prepared from HeLa cells treated with ERAL1 or non-targeted (control) siRNA for 72 h. After separation by centrifugation through 10–35% sucrose, the sample was divided into 17 fractions. Each fraction was analysed by western blotting using antibodies against the small (DAP3, MRPS22) and large (MRPL3) mitochondrial ribosomal subunits, ERAL1, COX II, TFAM, Lon and LRP130. (**C** and **D**) Ribosomal RNA levels of each fraction were analyzed by using real time PCR: 12S mitochondrial ribosomal RNA (C), 16S mitochondrial ribosomal RNA (D). The maximal value is 100% for each RNA.